

Building a Heterogeneous, Large Scale Morphable Face Model

Claudio Ferrari, *Member, IEEE*, Stefano Berretti, *Senior, IEEE*, Pietro Pala, *Senior, IEEE*, and Alberto Del Bimbo, *Senior, IEEE*

Abstract—3D Morphable Models (3DMMs) are powerful statistical tools for representing and modeling 3D faces. To build a 3DMM, a training set of fully registered face scans is required, and its modeling capabilities directly depend on the variability contained in the training data. Thus, accurately establishing a dense point-to-point correspondence across heterogeneous scans with sufficient diversity in terms of identities, ethnicities, or expressions becomes essential. In this manuscript, we present an approach that leverages a 3DMM to transfer its dense semantic annotation across a large set of heterogeneous 3D faces, establishing a dense correspondence between them. To this aim, we propose a novel formulation to learn a set of sparse deformation components with local support on the face that, together with an original non-rigid deformation algorithm, allow precisely fitting the 3DMM to arbitrary faces and transfer its semantic annotation. We experimented our approach on three large and diverse datasets, showing it can effectively generalize to very different samples and accurately establish a dense correspondence even in presence of complex facial expressions or unseen deformations. As main outcome of this work, we build a heterogeneous, large-scale 3DMM from more than 9,000 fully registered scans obtained joining the three datasets together.

Index Terms—3D Morphable Model, Sparse Component Learning, Dense Correspondence, 3D face reconstruction

1 INTRODUCTION

IN the field of 3D face analysis, one widely used statistical model that gained increasing interest throughout the years is the 3D Morphable Model (3DMM) [1]. Thanks to its ability to represent and manipulate 3D face shapes, it found successful application in a variety of tasks, spanning from computer graphics, to biometrics or medical imaging [2], [3], [4], [5], [6], [7]. In general, a 3DMM can be constructed by computing an average face and a set of *deformation components*, learned from an ensemble of fully registered face scans (*i.e.*, scans having a point-to-point semantic correspondence). Irrespective of the method employed to learn the components, their capability of warping the average face and generate plausible yet variegated novel 3D faces clearly depends on the variability contained in the training data. If learning is performed on small datasets with insufficient diversity, the model unlikely will be capable of generalizing to unseen, novel facial deformations [8]. So, it is a shared conviction that learning from *heterogeneous* and *abundant* data is decisive to go a step further [9].

In the context of face analysis, heterogeneity can be achieved by including both inter-subject variability in terms of gender, or ethnicity, and intra-subject changes due to pose, aging, expressions and topological variations (*e.g.*, mouth closed/mouth open). While for 2D images and videos the Web has been widely exploited as a natural source for collecting plentiful and variegated imagery, this is not the case for 3D data, which require dedicated and often expensive devices for acquisition. Consequently, in 3D, the need for larger amounts of heterogeneous data

can be answered by resorting to the union of different, existing datasets. However, acquisition devices used in different datasets are unlikely to share the same characteristics in terms of resolution or noise level, thus introducing an additional, unwanted level of variability. Further, while 2D image processing develops on the regular support given by the pixels grid, the irregular structure of 3D raw scans in terms of number and disposition of acquired points, demands for methods capable of establishing a dense, point-to-point correspondence across the scans.

A common and effective way to establish such dense correspondence is that of relying on a *prior* in the form of a prototypical 3D face model (template). The template can be non-rigidly deformed and put in dense correspondence with each scan so that, transitively, the scans are in dense correspondence each other. Despite the easy formulation, this is a challenging problem, where all the heterogeneity factors listed above come into play. However, notwithstanding the countless ways in which faces can vary, the deformations they can be subject to are yet constrained by the musculoskeletal structure and its anthropometric proportions. This prior knowledge is important in as much as it can be leveraged to ease the problem. A solution to exploit this information is that of using a 3DMM as template, which allows morphing the model to fit a target scan ensuring statistically plausible and face-like consistent deformations. Incidentally, we observe this is a *chicken-and-egg* problem, since the prior knowledge incorporated by the 3DMM is learned from a training set of face samples that need to be in dense correspondence. Therefore, in order to adapt to novel face shapes, a solution to expand the modeling capabilities of the 3DMM beyond those contained in the training data becomes essential.

Overall, accurately solving the above problem mainly

• C. Ferrari, S. Berretti, P. Pala and A. Del Bimbo are with the Department of Information Engineering, University of Florence, Florence, Italy, 50139. E-mail: claudio.ferrari@unifi.it

Manuscript received ; revised.

depends on two factors: (i) the extent to which the learned components can capture the variability contained in the training data and generalize to unseen samples; (ii) how well the fitting process can establish semantically meaningful associations between template and target. The majority of existing methods for components learning result in deformations that have global support on the face (the few exceptions are [6], [10]). This limits both the different shapes that can be generated when deforming the average face through a combination of the learned components, and the fitting capability of generalizing to unseen samples. For both (i) and (ii), spatial locality is arguably a desirable property that can increase the flexibility of the 3DMM [10].

In this paper, we provide original solutions to the above points (i)-(ii), and propose a new approach to establish a dense semantic correspondence between a large set of facial scans in different datasets. We start from the observation that the facial musculoskeletal structure induces neighboring vertices to move according to consistent patterns (principle of local consistency of motion). We leverage this property by first proposing a novel solution, called *Sparse Vertex Dictionary Learning*, to learn a per-vertex dictionary of primary deformation directions from a set of aligned training scans. Then, we estimate the optimal set of coefficients that allows reconstructing the training scans by expanding each learned primary deformation to a sparse set of vertices. The principle of local consistency of motion ensures each direction is expanded and applied to neighboring points, allowing us to model localized facial movements without the need of additional constraints. Such coefficients will constitute our Sparse and Locally Coherent (SLC) deformation components. This allows us to non-rigidly deform the 3DMM ensuring spatially-bounded yet coherent motions of vertices. The advantage is twofold: we adhere to the principle of local consistency of motion, thus respecting the facial anatomy; we can independently control the deformation of local neighborhoods, ultimately de-correlating complex facial movements. Then, we design a solution that uses the learned components to deform the average model to target faces by means of an iterative optimization, named *Non-Rigid Fitting* (NRF). Finally, we transfer the semantic annotation from the deformed model to target faces putting them in dense correspondence. A thorough experimentation in a set of different tasks on the FRGCv2.0, Bosphorus and FaceWarehouse datasets, shows the proposed solutions for components learning and registration can achieve performance that are comparable to those reported by state-of-the-art approaches, though we experiment our solution in the challenging cross-dataset scenario. From these datasets, we also construct our Heterogeneous Large-Scale 3DMM with capabilities at par of the best solutions in the literature.

In summary, the main contributions of this work are: (i) We propose a new solution for 3DMM construction that learns sparse and locally-consistent deformation components. These components augment the generalization capabilities of the model during fitting, and can be used to apply face deformations in an intuitive way; (ii) We design an iterative fitting strategy that combines together rigid and non-rigid model deformations. Remarkably, our method can operate independently from any landmark-based initialization; (iii) We use the approaches in (i) and

(ii) to densely align a large set of 3D face scans from heterogeneous datasets, and transfer the semantic annotation of the 3DMM to the target scans. Then, we use the registered scans to derive a Heterogeneous Large Scale 3DMM.

Finally, we point out this work shares some ideas with our preliminary investigations in [11], [12] and [13]. In [11], [12], we presented a solution to densely fit a 3DMM to raw face scans, and used the fitted 3DMM to synthesize new expressions by learning subject-independent deformation coefficients [13]. Though those works also developed on the idea of densely fitting a 3DMM to raw scans, the methods we propose here are original and substantially extend [11], [12]: (i) we propose the SLC component learning for 3DMM construction, instead of using the DL-3DMM in [8]; (ii) the fitting does not rely on any landmark-based initialization, and exploits an original procedure that does not resort to nearest-neighbor proximity; (iii) we perform annotation transfer from the 3DMM to the target scans that ultimately allows us to derive a heterogeneous large scale 3DMM.

The rest of the paper is organized as follows: In Section 2, we summarize the works in the literature that are more close to our proposed solution; In Section 3, we formulate a new approach for learning localized deformation components of a 3DMM; The 3DMM is then included in a framework for dense semantic annotation transfer in Section 4; Extended experimental results are reported in Section 5; Finally, discussion and conclusions are sketched in Section 6.

2 RELATED WORK

Constructing a 3DMM requires two main operations: Establishing group-wise dense correspondence between a training set of facial scans; Performing some statistical analysis on the registered data to derive an average model and a set of deformation components. In the following, we first revise the main approaches for these steps also evidencing their main limitations and differences with our solution; Then, we summarize the works that proposed a large-scale 3DMM.

Dense Correspondence between 3D Face Scans – Determining a dense correspondence between 3D point clouds can be seen as a particular case of a rigid/non-rigid registration problem. State-of-the-art methods can be categorized according to the fact they: (i) compute surface descriptors that can be used to define few landmarks of the face [14], [15], [16], [17], [18], perform region matching [19], [20], [21] or initialize a graph-matching procedure [22], [23]; (ii) resolve for an objective function to find a mapping between fiducial points [24], [25], [26], or (iii) use a 3D model of the face. In the following, we focus on the latter category being it the closest one to our proposed method. A more in depth discussion on the topic of dense face correspondence can be found in [27], [28], [29].

Several solutions used a 3D model of the face to transfer a set of reference labels on the model to a set of unlabeled scans. For example, this can be done by first establishing a sparse set of correspondences using landmarks of the face, then extending them to dense correspondences. For example, Paysan *et al.* [30] proposed a registration based on the non-rigid Iterative Closest Point (ICP) [24] algorithm. Since non-rigid ICP cannot handle large missing regions

and topological variations, facial expressions were not accounted for in this case. Gilani *et al.* [31] proposed to evolve level set curves with adaptive geometric speed functions to automatically extract seed points for dense correspondence. The method was refined in [32], where a multi-linear algorithm was used to establish dense point-to-point correspondence over a population of 3D faces varying in identity, facial expression and poses. Gilani *et al.* [33] proposed an algorithm that is based on the subsequent refinement of automatically detected sparse correspondences on the outer boundary of 3D faces. Fan *et al.* [34] proposed a *template* warping strategy to achieve semantic and topological correspondence. First a face is chosen as a template and used to initially provide a global alignment with the target faces using the Go-ICP [35], [36] algorithm. Then, preliminary correspondence and deformation from the template to the target are alternated and iterated for a few times to obtain a correspondence result that guarantees semantic association.

The most relevant trait that differentiates our solution with respect to the above works is that we jointly address landmark detection and dense registration, in difficult cross-dataset scenarios.

Constructing 3D Models of the Face – Two aspects have a major relevance in characterizing the different methods for 3DMM construction: (1) The human face variability captured by the training scans, which directly depends on their number, and heterogeneity; (2) The approach employed to learn the components. The former point is significant because if particular deformations do not appear in the training data, *e.g.*, facial expressions, the resulting 3DMM will not be capable of replicating such movements [8]. The second point, instead, determines to what extent the 3DMM is able to capture and reproduce the latent structure contained in the data. Most of the literature on 3DMM construction relies on the seminal work of Blanz and Vetter [1], who first presented a complete solution to derive a 3DMM by transforming the shape and texture from a training set of 3D face scans into a vector space representation based on PCA. This original 3DMM proposal was further refined into the Basel Face Model (BFM2009) by Paysan *et al.* [30]. A popular multi-linear 3D face model, called FaceWarehouse (FWH), that introduced expressive scans in the 3DMM training set was proposed by Cao *et al.* [37]. Further, some methods investigated different ways to learn the deformation components, like Thin-Plate Splines and Procrustes analysis [38], or multi-linear wavelets [39]. The Dictionary Learning-based 3DMM (DL-3DMM) presented in [8] is the most similar to our proposal, where a per-model dictionary of deformations is used to increase the modeling capabilities in case both identity and expression variations are present in the training data. However, all the above solutions cannot model local deformations. This happens because the deformations of different facial regions are highly correlated, due to the fixed anthropometric proportions and the structure of face parts. In addition, facial expressions are highly subject-dependent, often imply the concurrent movement of different facial regions, and significantly vary among different cultures [40]. In order to effectively deal with this complexity, as also discussed in [10], modeling facial deformations locally can increase the generalization capability of the 3DMM by decoupling facial

movements that are correlated with each other. For example, the expression “Surprise” is usually characterized by opening the mouth in conjunction with raising the eyebrows. If such movements do not appear separately in the training set, or they are not explicitly considered, statistical models will eventually reproduce them jointly because of their strong correlation. A method that exposed the capability of modeling local and spatially uncorrelated deformations is the work by Lüthi *et al.* [10], who generalized the PCA-based statistical shape model using a Gaussian Process 3DMM. While they discussed the importance of de-correlating facial movements to achieve more flexibility, the learned local deformations did not fully respect the anatomical structure, resulting in unnatural facial movements. Neumann *et al.* [6], instead, proposed a sparse variant of PCA with additional local support constraints to achieve localized and realistic deformations. They learned the deformations on mesh sequences of single subjects, and used them for artistic and animation purposes.

Recently, several solutions have been presented that apply Convolutional Neural Networks (CNNs) to learn non-linear 3D face models. These methods can regress shape and texture parameters directly from an input photo [41], or UV maps [42]. Some solutions added the capability of modeling extreme expressions using convolutional mesh autoencoders [43], [44] or using 4D sequences [45]. Liu *et al.* [46] learned a non-linear face model from a set of raw 3D scans using the PointNet architecture [47] to convert point clouds to identity and expression feature representations, while also establishing a dense point-to-point correspondence among them. Incidentally, this is the unique method in the literature that exhibits the capability of dealing with scans from different databases. However, the accuracy of the dense registration changes depending on whether target scans are included or not in the training data, which would require re-training the model for optimal results.

Large Scale Morphable Models – There are just few examples of morphable models constructed on large and heterogeneous datasets. The first 3DMM constructed on a large set of training examples was presented by Booth *et al.* [9], [25]. They introduced a Morphable Model construction pipeline to derive their Large Scale Facial Model (LSFM) from 9,663 distinct facial identities (about 12,000 scans in total), including variations in age, gender and ethnicity. However, all the scans were acquired in neutral facial expression from the same device. Further, the scan acquisition required a huge manual effort. Ploumpis *et al.* [48] presented a general approach to combine 3DMMs from different parts of an object class into a single 3DMM. They fused the variability and facial detail of the LSFM with the full head modelling of the Liverpool-York Head Model (LYHM) [49], thus creating the Combined Face & Head Model (CFHM). This provides a solution to the problem of combining existing models built using different templates that can only partly overlap, have different representation capabilities and are constructed from different datasets.

Differently from the few methods in the literature that construct large scale 3DMMs from the scans of one dataset [9], [25] (*i.e.*, acquired with the same device, so with same resolution, noise distribution, *etc.*), we prove our dense registration algorithm shows high generalization capabili-

ties that make it accurately work in cross-database scenarios, allowing large and heterogeneous data to be collected and effectively joined together. We underline this is a significant element in as much as all of the 3DMM learning solutions would benefit from the availability of more and variegated training data. The same advantage also holds with respect to [48], where cross-dataset capabilities were obtained but just *a posteriori* for two models, using a regressor to complete missing parts, and blending together covariance matrices from the models using a Gaussian Process.

3 LEARNING SPARSE AND LOCALLY COHERENT DEFORMATION COMPONENTS

The main idea behind the 3DMM is that of generating novel 3D faces by deforming a generic model \mathbf{m} through a linear combination of a set of deformation components \mathbf{C}_i :

$$\mathbf{S} = \mathbf{m} + \sum_{i=1}^k \mathbf{C}_i \alpha_i. \quad (1)$$

Although several alternatives to PCA have been proposed to learn such components, the common concept is that each \mathbf{C}_i should represent a statistically plausible shape deformation that needs to be consistent with the topology of human faces. We aim at deriving a set of deformation components that (i) model both identity and expression variations together, and (ii) affect only spatially bounded regions and are in compliance with the anatomical structure of the face. In this way, complex facial expressions can be reproduced combining different local deformations even if they do not explicitly appear in the training data. For this purpose, we developed a method based on a sparse decomposition of the training matrix, which ultimately allows us to learn localized but meaningful deformations. To ensure we can jointly model identity and expression variations, we made use of the registered models of the BU-3DFE dataset derived in [8] as our training data. Note that the BU-3DFE dataset contains only prototypical and global expressions.

3.1 Sparse Vertex Dictionary Learning

We represent the geometry of a 3D face as a vector $\mathbf{f}_i = [x_1, y_1, z_1, \dots, x_m, y_m, z_m]^T \in \mathbb{R}^{3m}$ that contains the linearized (x, y, z) coordinates of the m vertices. Let $\mathbf{F} = [\mathbf{f}_1, \dots, \mathbf{f}_N] \in \mathbb{R}^{3m \times N}$ be the matrix of the N training scans, each with m vertices arranged column-wise. Our goal is to extract from \mathbf{F} a set of sparse deformation components. To this aim, we compute the difference between each training scan and the average 3D face:

$$\mathbf{m} = \frac{1}{N} \sum_{i=1}^N \mathbf{f}_i, \quad \mathbf{v}_i = \mathbf{f}_i - \mathbf{m}, \quad \forall \mathbf{f}_i \in \mathbf{F}. \quad (2)$$

Each training sample \mathbf{v}_i now represents the set of vectors that transform the average model \mathbf{m} into a training model \mathbf{f}_i . Such \mathbf{v}_i will form our training matrix $\mathbf{V} = [\mathbf{v}_1, \dots, \mathbf{v}_N] \in \mathbb{R}^{3m \times N}$. We will refer to \mathbf{v}_i as *deformation field*.

In [8], it was shown how a dictionary of deformation components can be learned from the training data by solving an Elastic-net regression problem. This particular formulation includes both a sparsity L_1 penalty and an L_2

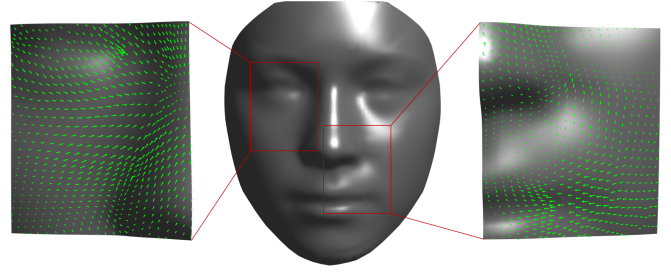


Fig. 1. Example of the locally coherent and smooth motion typical of human faces. The vector field \mathbf{v}_i (green arrows) depicts the difference between the average model and a scan of the training set.

regularization to prevent abrupt deformations. By defining $\ell_{1,2}(\mathbf{w}_i) = \lambda_1 \|\mathbf{w}_i\|_1 + \lambda_2 \|\mathbf{w}_i\|_2^2$, where λ_1 and λ_2 are, respectively, the sparsity and regularization parameters, the problem is formulated as:

$$\min_{\mathbf{w}_i, \mathbf{D}} \frac{1}{N} \sum_{i=1}^N \left(\|\mathbf{v}_i - \mathbf{D}\mathbf{w}_i\|_2^2 + \ell_{1,2}(\mathbf{w}_i) \right), \quad (3)$$

In this equation, the columns of the dictionary $\mathbf{D} \in \mathbb{R}^{3m \times k}$ are the deformation components, and $\mathbf{w}_i \in \mathbb{R}^k$ are the reconstruction coefficients of the k dictionary atoms. With this formulation, the learned dictionary represents the set of k deformation fields ($k \ll N$, each one of m vertices) that best reconstruct the input data. However, as per (3), the sparsity is imposed to the coefficients \mathbf{w}_i rather than to the dictionary \mathbf{D} . This implies the training data are being reconstructed using as few atoms as possible, but each atom \mathbf{D}_i has a global support on the face.

We adopted a novel, dual formulation of the dictionary learning problem, named Sparse Vertex Dictionary Learning: instead of targeting the reconstruction of the training data with the lowest number of dictionary atoms, we aim at using the lowest number of vertices within each atom. The sparsity penalty needs then to be applied on a per-vertex basis rather than a per-model basis. To this aim, we change the way we look at the training data: Instead of using the deformation fields \mathbf{v}_i as training samples, we use the displacement of each vertex coordinate with respect to the average, across all the N models. In other words, each training sample is now an N -dimensional data point, representing the statistics of the possible deformations each vertex coordinate is subject to across the N models, for a total of $3m$ training samples. Practically, this corresponds to taking the transpose of the data matrix, *i.e.*, $\mathbf{V}' = \mathbf{V}^T$, so that each sample becomes a vector $\mathbf{v}'_i \in \mathbb{R}^N$.

From (3), if $\mathbf{V}' \in \mathbb{R}^{N \times 3m}$, the resulting dictionary will be $\mathbf{D}' \in \mathbb{R}^{N \times k}$, and the coefficients \mathbf{w}'_i form a matrix $\mathbf{W}' \in \mathbb{R}^{k \times 3m}$. Under this perspective, the dictionary represents a basis containing the set of k ($k \ll 3m$) main directions of deformation that allow optimally reconstructing the training data. Instead, the coefficients \mathbf{w}'_i identify how to expand each direction \mathbf{d}_i to a localized set of vertices, and linearly combine them to reconstruct the deformation of the $3m$ coordinates in the N models. The meaningfulness of such expansion is ensured by the intrinsic local consistency of motion of the deviation fields \mathbf{v}_i induced by the underlying facial muscular structure. A qualitative example of

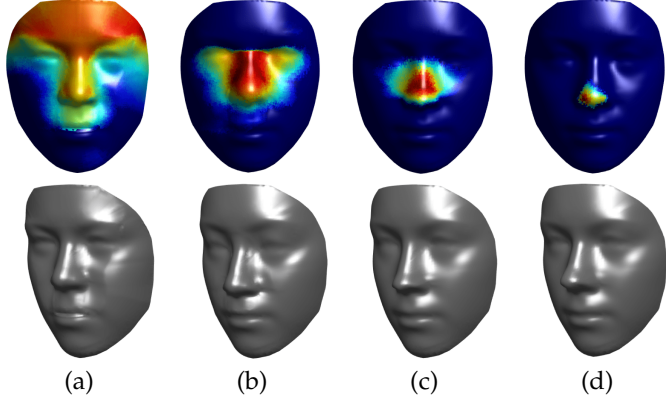


Fig. 2. Spatial extent of the deformation components (dark blue = no deformation). (a) $\lambda_1 = 0.1$, $\lambda_2 = 100$; (b) $\lambda_1 = 1$, $\lambda_2 = 1$; (c) $\lambda_1 = 1$, $\lambda_2 = 10$; (d) $\lambda_1 = 100$, $\lambda_2 = 0.1$.

this property is shown in Figure 1. Therefore, to reproduce the deformation of a spatially restricted patch, there is no need to know the exact motion of each point. Our learned dictionary summarizes the most significant directions of motion contained in the training data. Each entire model is then reconstructed by expanding each of the k directions to a localized set of vertices by means of the coefficients \mathbf{W}' .

3.2 Building the SLC-3DMM

Practically, the deformation fields \mathbf{v}_i include either positive or negative directions across the N models, *e.g.*, a nose might be shorter/thinner or longer/larger than the average one. To avoid the dictionary and coefficients, in addition to learn the vertex motions, also introduce unwanted redundancy, we force a positivity constraint. As reported in [50], forcing the positivity induces sparsity to the solution, while simultaneously promoting the complementarity of each learned atom. It is intended that opposite directions can be reproduced by multiplication for a negative value. Further, each deformation field likely contains opposite deformations occurring simultaneously in different facial regions, *e.g.*, as for the “Angry” expression, where to a raising of the upper lip, corresponds a lowering of the eyebrows. The positivity constraint allows decoupling such movements. To summarize, (3) becomes:

$$\begin{aligned} \min_{\mathbf{w}'_i, \mathbf{D}'} \frac{1}{3m} \sum_{i=1}^{3m} & \left(\|\mathbf{v}'_i - \mathbf{D}' \mathbf{w}'_i\|_2^2 + \ell_{1,2}(\mathbf{w}'_i) \right) \\ \text{s.t. } & \mathbf{D}' \geq 0, \quad \mathbf{W}' \geq 0. \end{aligned} \quad (4)$$

With this formulation, the $\ell_{1,2}$ term forces the algorithm to learn using as few vertices as possible, while encouraging smoothness to avoid discontinuities. The L_1 penalty and L_2 regularization terms interact with each other, both contributing to the definition of the spatial deformation extent, which allows controlling the behavior of the learned components. A qualitative example of the effect of varying λ_1 and λ_2 is shown in Figure 2.

To solve (4), we exploit the implementation in [51] that solves the problem by alternating the estimation of \mathbf{D}' and \mathbf{W}' , while keeping the other fixed. We chose this particular implementation for its efficiency and versatility (please refer to [51] for more details). After convergence, we use the

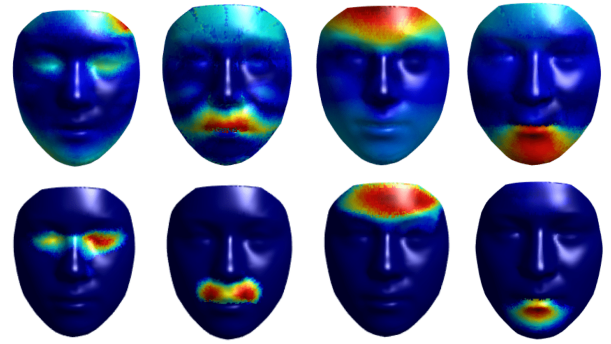


Fig. 3. Spatial deformation extent of the components \mathbf{C}_i learned without (top row) and with (bottom row) the positivity constraint in (4).

optimal coefficients of the reconstruction as deformation components: $\mathbf{C} = \mathbf{W}'^T$ (note that we take the transpose for convenience, so that $\mathbf{C} \in \mathbb{R}^{3m \times k}$). Some examples of components learned with and without the positivity constraint in (4) are shown in Figure 3. Without this restriction, although somewhat sparse, each component contains both negative and positive deformations, resulting in larger and spatially distant facial regions that are deformed. On the contrary, the positivity constraint eliminates this effect.

Finally, we observe that different facial regions can be more or less variable with respect to the average. Movable parts like the mouth or the eyes regions surely present a higher degree of variability compared to the forehead, and this gets reflected in the magnitude of the elements of \mathbf{D}' . However, this characteristic could change if different training scans are used. In order to account for this imbalance that could affect the model fitting, we compute the mean of the dictionary elements over the N models for each direction k_i , and define a weight vector $\boldsymbol{\mu} \in \mathbb{R}^k$ as $\boldsymbol{\mu} = \frac{1}{N} \sum_{i=1}^N D_{i,j} \forall j$. This represents the mean over each column, *i.e.*, the mean contribution of each direction. We will use this vector to regularize the deformation of the 3DMM, thus balancing the contribution of each component (Section 4.2). The sparse components \mathbf{C} , the average model \mathbf{m} and the weight vector $\boldsymbol{\mu}$ constitute our *Sparse and Locally-Coherent* (SLC)-3DMM.

4 DENSE SEMANTIC ANNOTATION TRANSFER

In this section, we describe our approach to non-rigidly deform a 3DMM to fit a target scan, thus transferring the 3DMM dense semantic annotation. First, in order to perform a meaningful fitting, the average model \mathbf{m} and a generic target point-cloud $\mathbf{t} \in \mathbb{R}^{h \times 3}$ need to be roughly aligned. To this aim, we first perform a rigid transformation to map the target shape into the space of the average model, accounting for 3D rotation, translation and scale. This can be done either using a set of sparse landmark pairs (if available), or performing a rigid ICP registration. We will use this latter solution in order to be independent from any additional constraint. Note that the alignment is performed with respect to \mathbf{m} , thus bringing point clouds from different datasets into the same coordinate system. For clarity of notation, since the fitting process operates by iteratively deforming the average model, from now on we will refer to it as \mathbf{S} (see (1)), and to coarsely aligned point-clouds as $\hat{\mathbf{t}}$.

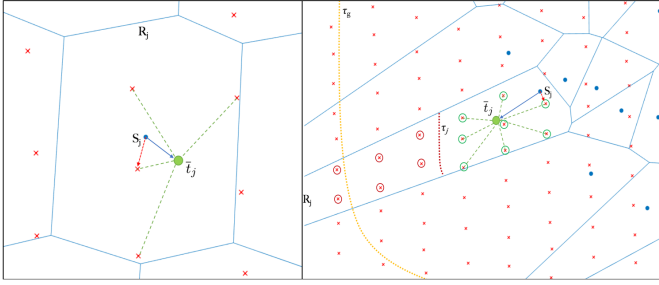


Fig. 4. Local Mean-Point association and outliers rejection. For each Voronoi region R_j (blue polygon) defined by S , the point S_j (blue dot) is associated to the centroid \bar{t}_j (green dot) of the points \hat{t}_{R_j} (red crosses). The local and global rejection thresholds (red and yellow dotted lines) are iteratively updated to progressively adapt to the global shape.

4.1 Establishing Point-to-Point Correspondence

In order to deform S to match a target model \hat{t} , a preliminary correspondence between points in \hat{t} and S must be established. However, the general shape difference between the average model and the target point-cloud can be significantly large, mostly because of the presence of facial expressions and unseen identities. Therefore, the initial correspondence is likely to be far from optimal. Pairing each vertex of S to one in \hat{t} is the core of the whole procedure, as the 3DMM is deformed under the guidance of such point-to-point correspondence. The most straightforward solution to achieve this would be associating each point in S to its nearest-neighbor (NN) in \hat{t} , deforming S , and repeating these two steps until convergence. However, several inconveniences might arise: (i) Due to non-uniform regions and different density of points, multiple vertices of \hat{t} might be paired with the same point in S and vice versa; (ii) Depending on the density of points in \hat{t} , the per-vertex Euclidean distance with respect to S can be small. Hence, the minimization can converge after few iterations to a suboptimal solution; (iii) Points in \hat{t} that are identified as outliers, might instead correctly belong to the face surface but be far apart from any point of S , if the template's general shape differs significantly from the target. To address such problems, we formulated a joint mean-point association and adaptive outliers rejection strategy. In the following, we separately describe each step along with its rationale.

4.1.1 Local Mean Point Association

With the aim of both avoiding duplicated associations and selecting proper points to allow an iterative refinement of the 3DMM, we sketched the point-to-point association strategy complying with the following observations:

- Multiple vertices $\hat{t}_{R_j} = \{\hat{t}_i, \dots, \hat{t}_k\} \in \hat{t}$ sharing the same nearest-neighbor $S_j \in S$, belong to the Voronoi region R_j defined by S_j ;
- Low curvature regions can be approximated with piecewise-planar surfaces;
- For high curvature regions, the closest point scheme might not reflect the local surface properties [52];
- Scanners usually induce high-frequency noise that would be desirable to attenuate.

Based on the observations above, our point-to-point associations operates by mapping each vertex S_j to the centroid \bar{t}_j

of the vertices $\hat{t}_{R_j} = \{\hat{t}_i, \dots, \hat{t}_k\}$ belonging to the Voronoi region R_j of S_j . Note that R_j can contain either a single or any number of points.

A key problem at this stage is that of handling possible outliers that could impair the correct estimation of \bar{t}_j . Those are frequently associated to contour points, whose Voronoi regions are not bounded, and those containing holes. To account for that, we estimate both a global and a local rejection threshold. The global threshold τ_g is computed as $\tau_g = \bar{d} + \sigma_d$, where \bar{d} is the average NN-distance between S and \hat{t} , and σ_d is the standard deviation. Each local threshold τ_j is computed in the same way as the global threshold, considering separately points \hat{t}_{R_j} belonging to each Voronoi region. The centroids \bar{t}_j are then computed after the global and local thresholding, and mapped at position j in the re-indexed model \hat{t}^c . Figure 4 exemplifies the procedure.

This strategy has the advantage of letting S iteratively adapt to the global shape of \hat{t} by avoiding getting attached to the closest points, yet maintaining the geometrical properties of the surface. It also indirectly handles cases where distinct points of S share the same nearest-neighbor in \hat{t} . However, points of S in correspondence of the boundary or holes in the surface of \hat{t} might have missing associations, as effect of the global and local thresholding. Though, we cannot leave them over as the same occurs, for example, around the mouth region when it is open. In order to correctly deform S and adapt to such facial movements, we want them to be paired.

4.1.2 Association Refinement

Once the mean-point association procedure is completed, the majority of the points of S have been paired with the centroids \bar{t}_j of the Voronoi regions R_j . We now consider the points of S not yet paired with any point in \hat{t} . The effect of possible residual outliers and duplicates is now considerably reduced, as the majority of them have been handled. The final association refinement is achieved by computing, for each non-paired point of S , the nearest-neighbor in \hat{t} , and mapping the indices of the nearest-neighbors $idx_{\hat{t}}$ to their corresponding locations idx_S in the re-indexed model \hat{t}^c . At the end of the process, each point of S is paired. This ensures the uniqueness of the association, leading to a model \hat{t}^c with a unique point-to-point correspondence to S . The pseudo-code for the procedure is summarized in Algorithm 1.

4.2 SLC-3DMM Deformation by Non-Rigid Fitting

In order to deform S to accurately match \hat{t}^c a novel approach, namely, Non-Rigid Fitting (NRF) is adopted. The point-to-point correspondence that results from the initial ICP registration is refined to re-align \hat{t}^c to S by estimating an orthographic similarity transformation:

$$S = \hat{t}^c \cdot P + T, \quad (5)$$

where $T \in \mathbb{R}^3$ is the 3D translation, and $P \in \mathbb{R}^{3 \times 3}$ contains the 3D rotation and scale parameters. P is found in closed-form solving the following least squares problem:

$$\arg \min_P \|S - \hat{t}^c \cdot P\|_2^2. \quad (6)$$

Algorithm 1: Point-to-Point Correspondence

Input: Deformed Model \mathbf{S} , Target Shape $\hat{\mathbf{t}}$
Output: Re-indexed Model $\hat{\mathbf{t}}^c$

```

1  $\hat{\mathbf{t}}^c = \text{ZerosLike}(\mathbf{S});$  // Initialize  $\hat{\mathbf{t}}^c$ 
2  $\tau_g = \text{ComputeThreshold}(\mathbf{S}, \hat{\mathbf{t}});$ 
/* Section 4.1.1 */
3 foreach  $S_j \in \mathbf{S}$  do
4    $[R_j, \hat{t}_{R_j}] = \text{ComputePointsVoronoiRegion}(S_j, \hat{\mathbf{t}});$ 
5    $\tau_j = \text{ComputeThreshold}(S_j, \hat{t}_{R_j});$ 
6    $\hat{t}_{R_j} = \text{RemoveOutliers}(\hat{t}_{R_j}, \tau_g, \tau_j);$ 
7   if  $\hat{t}_{R_j} \neq \emptyset$  then
8      $\bar{t}_j = \text{ComputeCentroid}(\hat{t}_{R_j});$ 
9      $\hat{\mathbf{t}}^c(j) = \bar{t}_j;$  // Assign  $\bar{t}_j$  to  $\hat{\mathbf{t}}^c$  at index  $j$ 
10     $\mathbf{S} = \text{RemoveVertices}(\mathbf{S}, j);$  // Remove  $S_j$  from  $\mathbf{S}$ 
/* Section 4.1.2 */
11  $[idx_S, idx_{\hat{\mathbf{t}}}] = \text{NNSearch}(\mathbf{S}, \hat{\mathbf{t}});$ 
12  $\hat{\mathbf{t}}^c(idx_S) = \hat{\mathbf{t}}(idx_{\hat{\mathbf{t}}});$ 

```

Algorithm 2: Non-Rigid Fitting (NRF)

Input: Average Model \mathbf{m} , Sparse Components \mathbf{C} , Weights μ , Target Shape \mathbf{t} , Error Threshold τ_e , Iterations Limit I_l
Output: Deformed Model \mathbf{S}

```

1  $\hat{\mathbf{t}} = \text{ICP}(\mathbf{t}, \mathbf{m});$ 
2  $err = \text{ComputeEuclideanError}(\hat{\mathbf{t}}, \mathbf{m});$ 
3  $\mathbf{S} = \mathbf{m}, i = 0, \delta_e = \tau_e + 1$ 
4 while  $i < I_l \parallel \delta_e > \tau_e$  do
5    $\hat{\mathbf{t}}^c = \text{P2PCorrespondence}(\mathbf{S}, \hat{\mathbf{t}});$  // Algorithm 1
6    $[\hat{\mathbf{t}}^c, \hat{\mathbf{t}}] = \text{SimilarityTransform}(\hat{\mathbf{t}}^c, \hat{\mathbf{t}}, \mathbf{S});$  // Eq. (5), (6), (7)
7    $\mathbf{S} = \text{SLCFitting}(\hat{\mathbf{t}}^c, \mathbf{S}, \mathbf{C}, \mu);$  // Eq. (8), (9)
8    $e = \text{ComputeEuclideanError}(\hat{\mathbf{t}}, \mathbf{S});$ 
9    $\delta_e = err - e;$ 
10   $err = e;$ 
11   $i = i + 1;$ 

```

A solution to this equation is given by $\mathbf{P} = \mathbf{S} \cdot \hat{\mathbf{t}}^c$, where $\hat{\mathbf{t}}^c$ is the pseudo-inverse of $\hat{\mathbf{t}}^c$. The translation is then recovered as $\mathbf{T} = \mathbf{S} - \mathbf{P} \cdot \hat{\mathbf{t}}^c$. Rotation and scale matrices $[\mathbf{R}, \mathbf{S}_c] \in \mathbb{R}^{3 \times 3}$ can be retrieved applying QR decomposition to \mathbf{P} , thanks to the orthogonality property of any general rotation matrix, *i.e.*, $\mathbf{R}^T = \mathbf{R}^{-1}$. Using $[\mathbf{R}, \mathbf{S}_c]$ and \mathbf{T} , we re-align both $\hat{\mathbf{t}}^c$ and $\hat{\mathbf{t}}$ to \mathbf{S} prior to performing the deformation:

$$\hat{\mathbf{t}}^c = (\hat{\mathbf{t}}^c \cdot \mathbf{R}) \cdot \mathbf{S}_c + \mathbf{T}. \quad (7)$$

To deform \mathbf{S} , we need to find the optimal set of deformation coefficients $\alpha \in \mathbb{R}^k$ so that the per-vertex distance between the two point sets is minimized. Similar to other works using a morphable model [8], [33], [34], we formulate the problem as a regularized least-squares:

$$\min_{\alpha} \|\hat{\mathbf{t}}^c - \mathbf{S} - \mathbf{C}\alpha\|_2^2 + \lambda \|\alpha \circ \mu^{-1}\|_2, \quad (8)$$

where λ is the regularization parameter that allows balancing between the fitting accuracy and smoothness of the deformation. Recalling the definition of μ in Section 3.2, here we regularize the deformation using the inverse μ^{-1} so that the contribution of each component is weighed with respect to its average intensity. By pre-computing $\mathbf{X} = \hat{\mathbf{t}}^c - \mathbf{S}$, the solution is found in closed form:

$$\alpha = (\mathbf{C}^T \mathbf{C} + \lambda \cdot \text{diag}(\hat{\mu}^{-1}))^{-1} \mathbf{C}^T \mathbf{X}, \quad (9)$$

where $\text{diag}(\hat{\mu}^{-1})$ denotes the diagonal matrix with vector $\hat{\mu}^{-1}$ on its diagonal. \mathbf{S} is then deformed applying (1).

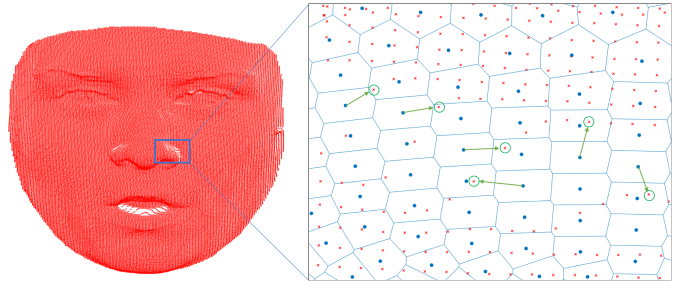


Fig. 5. Distinct points in \mathbf{S} (blue dots) can be associated to the same point in $\hat{\mathbf{t}}$ (red dots). This occurs in less dense regions, when Voronoi regions are empty.

Finally, we estimate the per-vertex error of the deformed model as the average Euclidean distance between each vertex of \mathbf{S} and its nearest-neighbor in $\hat{\mathbf{t}}$. Note that the error is not estimated with respect to the corresponded mean-point model $\hat{\mathbf{t}}^c$ (as seen in Section 4.1 using that model is advantageous during the deformation to prevent incorrect point-to-point associations and account for large topological differences). Here, the error is computed with respect to $\hat{\mathbf{t}}$, thus ensuring the deformation process terminates when the two surfaces are, on average, as similar as possible.

The whole pipeline is repeated until the error between subsequent iterations is above some threshold τ_e , or a maximum number of iterations is reached. The pipeline is sketched in Algorithm 2. At this point, the 3DMM has been optimally fit to the target shape, and we can transfer the semantic labeling of \mathbf{S} to $\hat{\mathbf{t}}$.

4.3 Transfer the Semantic Annotation

To transfer the dense semantic annotation, each point of \mathbf{S} must be associated to a distinct point in $\hat{\mathbf{t}}$, so that the latter has the same semantic indexing of the morphable model. In other words, we want to find a permutation of a subset of the h vertices of $\hat{\mathbf{t}}$ such that they match our labeling structure. For this reason, we again need to account for distinct points of \mathbf{S} having the same nearest-neighbor in $\hat{\mathbf{t}}$ (the duplicates). Figure 5 shows a visual example of this problem occurring. Addressing this issue allows obtaining a smoother mesh. Similarly to Section 4.1.2, this step is achieved by computing, for each vertex in \mathbf{S} , the nearest neighbor in $\hat{\mathbf{t}}$. Vertices of \mathbf{S} having a unique nearest-neighbor can be directly put in correspondence. Those having duplicated associations are handled by iteratively removing from both $\hat{\mathbf{t}}$ and \mathbf{S} the vertices that correspond to the unique indices $idx_{\hat{\mathbf{t}}}^{un}$ and idx_S^{un} of minimum distance, and repeating the nearest-neighbor search until no more points in \mathbf{S} have a missing counterpart in $\hat{\mathbf{t}}$. At each iteration, before removing the vertices and seeking new correspondences, the vertices $\hat{\mathbf{t}}(idx_{\hat{\mathbf{t}}}^{un})$ are re-indexed to new locations $\hat{\mathbf{t}}(idx_S^{un})$, so that they correspond to the semantic labeling structure of the 3DMM. The process ends when all points in \mathbf{S} have been paired, as summarized in Algorithm 3.

5 EXPERIMENTAL RESULTS

We carried out an extensive experimental validation to showcase the quality of our solution under different perspectives. To this end, in the following, we first describe

Algorithm 3: Semantic Annotation Transfer

```

Input: Deformed Model  $S$ , Target Shape  $\hat{t}$ 
Output: Re-indexed Model  $\hat{t}'$ 

1  $\hat{t}' = \text{ZerosLike}(S)$ ; // Initialize  $\hat{t}'$ 
2 while  $S \neq \emptyset$  do
3    $[idx_S^{un}, idx_{\hat{t}}^{un}] = \text{FindUniqueMinimumNN}(S, \hat{t})$ 
4    $\hat{t}'(idx_S^{un}) = \hat{t}(idx_{\hat{t}}^{un})$ ;
5    $S = \text{RemoveVertices}(S, idx_S^{un})$ ;
6    $\hat{t} = \text{RemoveVertices}(\hat{t}, idx_{\hat{t}}^{un})$ ;

```

the datasets used for evaluation and the preprocessing operations applied to the data (Section 5.1). Then, in an ablation study, we investigate the effect induced by the individual components of our solution and by different parameter setting (Section 5.2), we show the fitted model preserves identity information that allows using it in 3D face recognition (Section 5.3), and evaluate our approach in the task of 3D landmark localization also in comparison with state-of-the-art-solutions (Section 5.4). Finally, we propose the construction of a 3DMM on a large set of training data collected across heterogeneus datasets (Section 5.5).

5.1 Datasets

In the experiments, we used three benchmarks that cover a wide range of different characteristics for 3D faces: the Face Recognition Grand Challenge (FRGCv2.0) [53], the Bosphorus [54], and the FaceWarehouse [55] datasets. A fourth dataset, the Binghamton University 3D Facial Expression dataset (BU-3DFE) [56], was used for training our morphable model, so we did not include it in the experiments.

FRGCv2.0 – It is composed of 466 individuals, for a total of 4,007 scans collected in two separate sessions. Approximately, 40% of the scans show slight spontaneous expressions. On average, the FRGCv2.0 scans have $35K$ vertices on the face region. Scans are obtained with a high-resolution Minolta Vivid 900/910 sensor.

Bosphorus – This dataset comprises 4,666 high-resolution scans of 105 individuals. There are up to 54 scans per subject, which include prototypical expressions, facial action units activation, rotations and occlusions. Scans in the Bosphorus dataset have been captured with a structured-light scanner with an average of $30K$ vertices on the face region (similar to FRGCv2.0). This dataset also contains rotated and occluded scans, that we did not use. In fact, in rotated scans, no points exist for self-occluded regions, making the dense correspondence ambiguous. The same applies for occluded scans, where points corresponding to occluded regions do not belong to the face surface. For the sake of completeness, we conducted a qualitative and quantitative evaluation on these subsets that can be found in the supplemental material.

FaceWarehouse – This dataset comprises 3,000 Kinect RGB-D sequences of 150 individuals, aged 7-80. For each individual, 20 sequences are captured that include the neutral expression plus 19 natural expressions such as mouth-opening, smiling, kissing, etc. The data that have been released for public use consist of the first RGB-D frame of each sequence. The resolution of the point-clouds extracted from the depth frames is of about $15K$ vertices.

Parameter Settings – For all the reported experiments, the error threshold τ and the maximum number of iterations in Algorithm 2 have been set to 0.01 and 30, respectively. The regularization parameter λ of (9) was set to 1. The SLC-3DMM used in this work has 6,704 vertices.

Computational Time – A MATLAB implementation on a machine with Xeon CPU (2.6GHZ, single thread), processes the whole pipeline in approximately 40 seconds, against 100 and 160 seconds as reported, respectively, in [19] and [34], on a similar hardware.

5.1.1 Pre-Processing

FRGCv2.0, Bosphorus and FaceWarehouse exhibit very different characteristics. In order to extract the facial region in a consistent way across these datasets, we exploit the RGB face images to identify 69 fiducial points using the landmark detector by Bulat *et al.* [57]. Then, we map the detected landmarks to the 3D data exploiting the alignment of the RGB-D frames for FRGCv2.0, and FaceWarehouse or the texture mapping for Bosphorus. Landmarks are first used to locate the nose tip, whose location is refined looking for the point with largest z value within a neighborhood. Following a standard convention, to crop the face region we define a sphere of radius r centered at the nose tip. However, cropping the face using this methodology can lead to the inclusion of noisy regions such as those of neck or ears. In addition, this does not take into account the global shape of the face, which can vary significantly across gender, age or ethnicity. Further, for different datasets, the optimal r might be different. Thus, to extract the facial contour, we estimate the convex-hull of the face based on the landmarks of the facial boundary. To include the forehead region that would be cut out due to the absence of landmarks, we estimate the sphere radius r as the distance from the nose tip to the farthest boundary landmark. We then crop all the points within the union of the sphere and the convex-hull defined by the landmarks. In this way, we also include the forehead region, while maintaining the correct face shape. Finally, we observe that the absence of some landmarks does not compromise the success of the procedure. In this case, we detect the nose tip and use the sphere-based method.

5.2 Ablation Study

In the following, we aim at delving into the details of the proposed learning approach (SLC) and registration algorithm (NRF). We first evaluate the fitting accuracy obtained by applying our NRF procedure (Algorithm 2) with various configurations of the SLC-3DMM, and analyze the impact of the learning parameters λ_1 , λ_2 , and k (Section 5.2.1). We then show our SLC components can be intuitively controlled by exploiting their local nature, and used to manipulate a 3D face (Section 5.2.2).

5.2.1 SLC Parameters

As discussed in Section 3.2, λ_1 and λ_2 mainly define the spatial extent of each component. Both $L1$ and $L2$ regularization are applied while learning the components C , which expand each of the k learned directions d_i to a set of local vertices. In general, the $L2$ regularization leads to vectors with small elements, and the higher the value of the

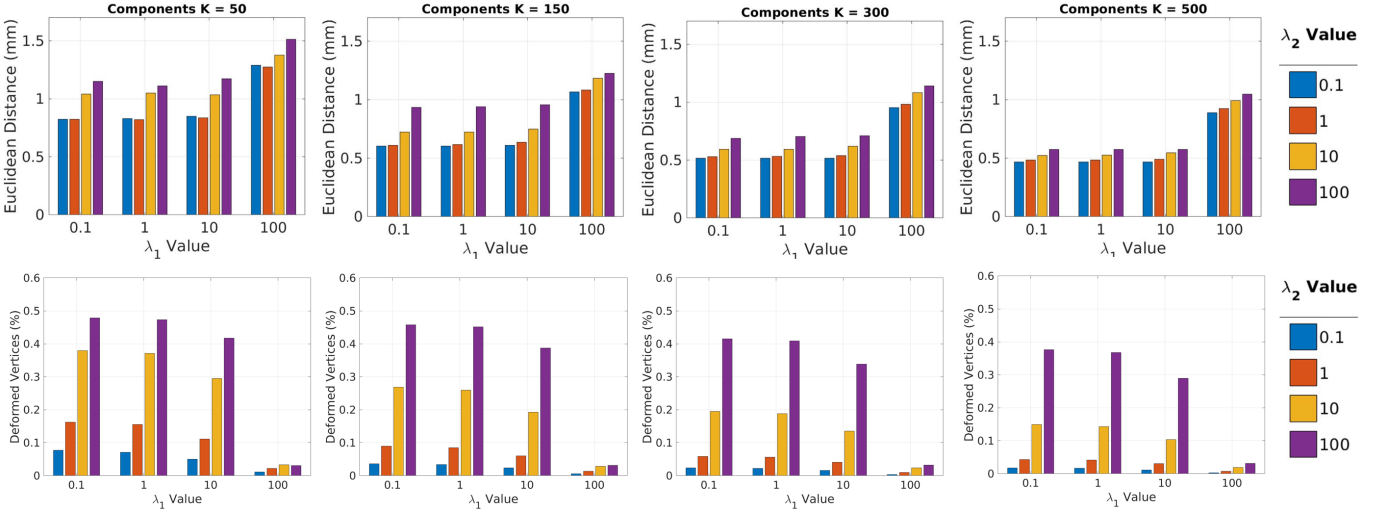


Fig. 6. Sensitivity analysis on the SLC parameters. Plots in the top row report the per-vertex error obtained on a sample of 200 scans from the FRGCv2.0 database applying Algorithm 2 with SLC components learned varying λ_1 and λ_2 . In the bottom row, the average proportion of deformed vertices with respect to the learning parameters λ_1 and λ_2 are reported. Each plot reports a different k .

parameter λ_2 , the smaller the elements of \mathbf{C} . Assuming λ_1 is kept fixed, larger λ_2 values imply that a greater number of small, yet not null, entries of \mathbf{C} can be retained at the same cost. This yields both to a larger area that is deformed and to a smoother transition to zero-valued elements. On the opposite, larger λ_1 values increase the cost of each non-zero element. Ultimately, this leads to components where abrupt transitions to zero-valued elements might occur. The best choice of such parameters can follow two observations: (i) the spatial extent of the deformation needs to be sufficiently limited so that each facial region can be deformed independently. This also helps to maintain the founding concept of local consistency of motion; (ii) we still want to have enough large and smooth transitions so that different components can interact without introducing irregularities (see Figure 2).

In Figure 6 (top row), we report the reconstruction error obtained by applying Algorithm 2 to a subset of 200 scans of the FRGCv2.0, using components learned varying λ_1 , λ_2 and k . The error is computed as the average per-vertex, nearest neighbor Euclidean distance between the fitted model \mathbf{S} and $\hat{\mathbf{t}}$. First, we can see that the per-vertex error is generally low, and inversely proportional to the number of components k . Whereas more components allow modeling complex facial deformations, which can be helpful in generating more variegated face shapes, we also observed that, despite the slightly lower error, it can lead to less smooth fitted models, as effect of the interaction between components. Parameters λ_1 and λ_2 , instead, behave consistently across different k . As expected, larger errors are observed when there is a discrepancy between the two values, as discussed above. For each k , the highest per-vertex error is obtained when λ_2 is very large ($\lambda_2 = 100$), in accordance to our assumption that each component should be spatially bounded. The error decreases when the two parameters are balanced and kept stable to lower values (< 10), so that sufficiently small regions are smoothly deformed. Note that the absolute value of the parameters weighs more than their ratio when learning the components. Indeed, a much

larger error is observed, for example, when $\lambda_1 = 100$ and $\lambda_2 = 10$ (1 : 10) with respect to $\lambda_1 = 10$ and $\lambda_2 = 0.1$ (1 : 100). This suggests excessively large deformations (λ_2) imply undesired interactions, whereas smaller, non-smooth deformations (λ_1) can induce irregularities. Figure 6 (bottom row) reports a quantitative evaluation of the spatial deformation extent; the bar plots show the average proportion of vertices that are activated by the components \mathbf{C} . Such proportion varies approximately from 50% to 5%.

Depending on the application of interest, it is possible to exploit such versatility and choose the most proper configuration. For example, if the goal is to synthetically generate natural looking and variegated meshes, one can choose to use larger values of k and λ_2 . Since our main goal is to densely register together a large number of heterogeneous scans, we privileged a configuration ensuring higher smoothness. So, unless otherwise stated, we employed a SLC configuration with $k = 50$, $\lambda_1 = 10$, $\lambda_2 = 1$.

5.2.2 Controlling the SLC Components

In the following, we show that the local and anatomically meaningful nature of the SLC components can be exploited to manipulate a 3D face in an intuitive way. Each component \mathbf{C}_i applies a deformation to a spatially restricted region; Thus, we can select which component to use depending on the area of the face we wish to warp. To show this, we choose one control vertex m_c in the average model, select the subset of k^* components ($k^* < k$) that are not null in m_c , and deform \mathbf{m} with a single or a combination of some of the selected k^* components. In order to highlight the fact only a subset of the components has effect on different face areas, for this application we set $k = 300$. Considering 14 landmarks corresponding to significant areas of the face [14], the average number of active SLC components in correspondence of each one is $k^* = 86$ out of $k = 300$. Figure 7 shows a qualitative example on two of these landmarks, *i.e.*, nasal root and mouth corner. Note the SLC components (top two rows) affect only the region surrounding the control point, yet resulting in natural looking deformations. The

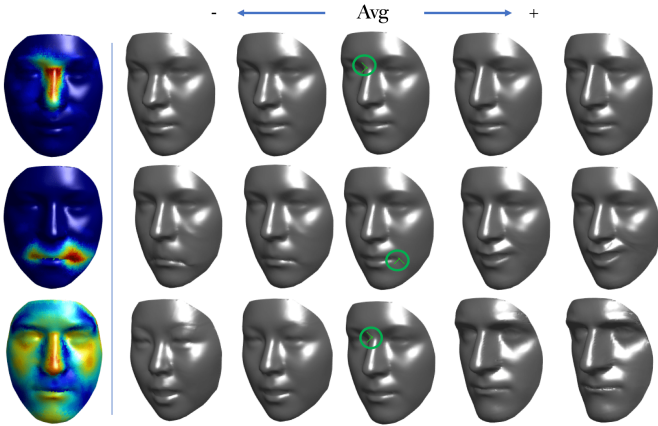


Fig. 7. The average model can be locally deformed by selecting one or more control points. SLC components (top two rows) affect the region around the control point (green circle). The PCA model (bottom row) affects the whole shape.

standard PCA model (bottom row), instead, deforms the whole shape. This is a valuable property of our model that can be employed in different ways. Similarly to Neumann *et al.* [6], a user could use a graphical interface to select a point of the face and visualize all the possible applicable deformations, then choose which one to apply.

5.3 3D Face Recognition

We further evaluated the faithfulness of the deformed shapes \mathbf{S} obtained with the proposed SLC-3DMM and NRF procedures, with respect to the original ones $\hat{\mathbf{t}}$ in the task of 3D face recognition. To this aim, we exploited the deep Vgg-16 network of Kim *et al.* [58]. They fine-tuned the VggFace [59] on a multitude of depth images from a variety of 3D face datasets, obtaining remarkable recognition accuracies. In this experiment, we aim at comparing the Rank-1 accuracy that is attained using the original depth images with respect to those obtained by rendering as a depth image each fitted shape \mathbf{S} . We find using a deep convolutional network for this purpose particularly useful, as the recognition is achieved grounding solely on the visual similarity between the images. We tested on the Bosphorus dataset as the others were used in [58] to train the network. For this particular application, which requires higher fitting accuracy, we set the number of components to $k = 300$.

We generated the depth images exploiting the publicly available code in [58]. For the experiments, we followed the procedure described in [58], and split the scans in gallery and probe, according to three protocols: Neutral vs. Neutral (N vs N), Neutral vs. Non-Neutral (N vs NN) and Neutral vs. All (N vs A). In all the three cases, the gallery is composed of the first neutral scan of each identity (105 subjects). The probe set is instead either composed of neutral scans only (N vs N), expressive scans only (N vs NN), both neutral and expressive scans (N vs A). The deep network is used to extract a 4096-dimensional face descriptor $\mathbf{f} \in \mathbb{R}^{4096}$ from each image. The identification is then performed by computing the cosine similarity $s = \frac{\mathbf{f}_i \cdot \mathbf{f}_j}{\|\mathbf{f}_i\| \cdot \|\mathbf{f}_j\|}$ between gallery and probe descriptors, and selecting the gallery sample with maximum similarity. Note that both probe and

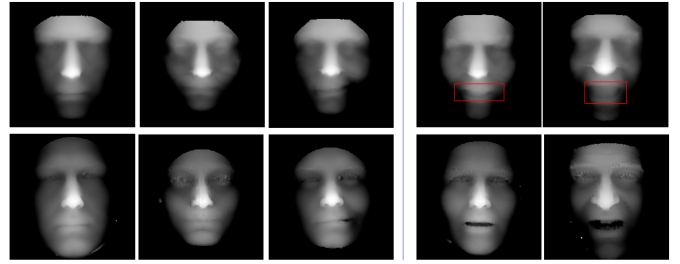


Fig. 8. Depth images generated using the code of [58]. Our fitted shapes \mathbf{S} (top row) and the originals (bottom row). The rendering causes uniform texture inside the mouth regions of our shapes (red rectangles).

TABLE 1
Rank-1 recognition accuracy on Bosphorus comparing the original depth images and our generated shapes \mathbf{S}

Method	N vs N	N vs NN	N vs A
Original	98.7	95.0	95.3
NRF	96.7	83.3	84.2

gallery contain either the original scans or the fitted models \mathbf{S} . Results are reported in Table 1.

In the N vs N scenario, the drop of accuracy is very small, indicating the precision and consistency of our fitting across different identities. In the other protocols, we observed a drop in the accuracy. Analyzing the wrongly classified examples, we found the vast majority of the misclassifications being relative to examples where expressions cause mouth or eyes opening. These regions in the original depth images include details, such as teeth, or eyebrows that are not included in our mesh by construction and are rendered as uniform texture, which have likely compromised the face descriptors. Some examples are shown in Figure 8. However, we can see expressions were correctly modeled during the fitting. Despite this issue, recognition results show our method can correctly fit the facial surface across different individuals, capturing the relevant traits of the identity and accounting for large expressions.

5.4 Landmarks Detection

In this section, we report a comparison between our proposed dense registration method against standard techniques in a landmark detection task. Since our proposal consists of a combination of a novel method for learning the 3DMM components (SLC) and a point-to-point association strategy (mean-point association plus NRF that we refer as *Ours* in the following), we compare against methods falling in either one of the categories. First, to assess the contribution of our proposed mean-point association, we substituted Algorithm 1 from our pipeline, with the nearest-neighbor strategy for point-to-point association as proposed in [11], [12]. This solution is called NRF+NN+SLC in the following. Further, we compared against two standard non-rigid point-cloud matching techniques: the Coherent Point Drift (CPD) [60] and Non-Rigid ICP (NICP) [24] algorithms. Finally, we explored the behavior of the classic PCA-based 3DMM and the DL-3DMM in [8], which is the most similar to our proposal, when used in place of the proposed SLC. In the following, these two solutions are called, respectively,

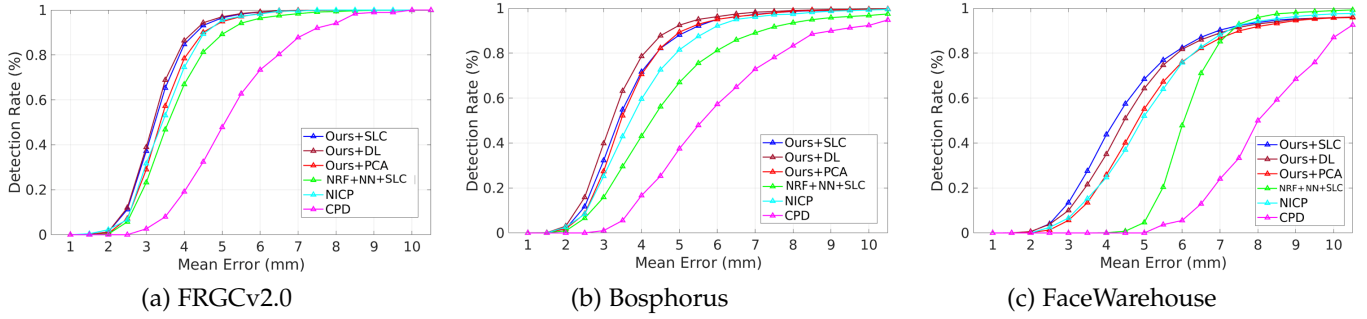


Fig. 9. Cumulative landmark localization error distributions for (a) FRGCv2.0, (b) Bosphorus, (c) FaceWarehouse.

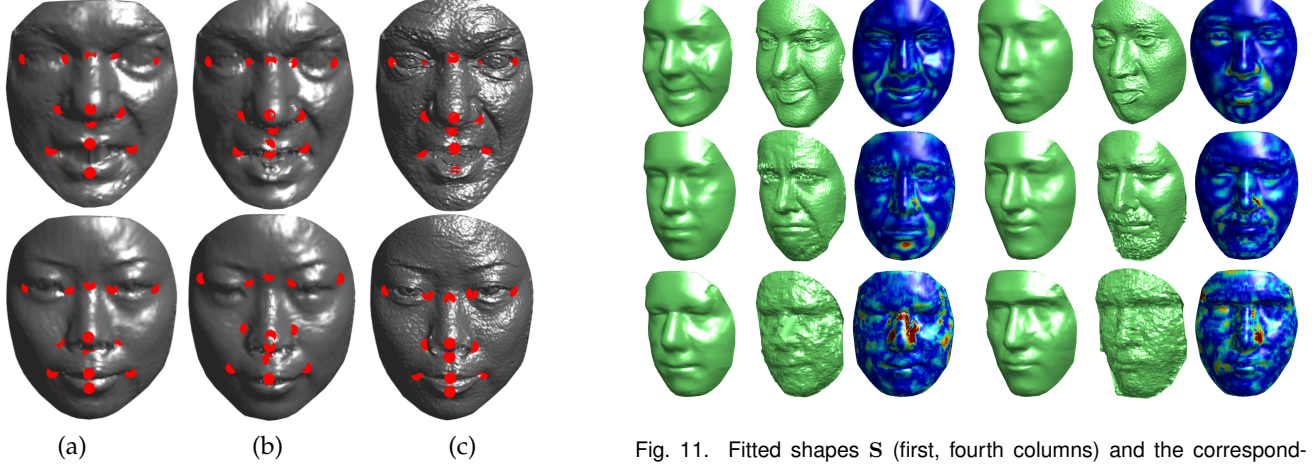


Fig. 10. Comparison between the re-indexed models t' obtained using the proposed mean-point association (a) with respect to the standard Nearest-Neighbor solution (b). The ground-truth scans are shown in (c).

Ours+PCA and Ours+DL. For the PCA and DL variants, we chose the best configurations as reported in [8], where a detailed analysis was conducted. Following a common practice, we report results in terms of landmark localization error, which is a well-established measure to assess the validity of face fitting. To evaluate the error, we first manually labeled a landmark configuration on the average model \mathbf{m} , obtaining a set of indices L_{idx} . The error is then computed between the ground-truth annotations in $\hat{\mathbf{t}}$ provided by [14], [55], and our transferred landmark annotation obtained applying the full pipeline, *i.e.*, $\hat{\mathbf{t}}'(L_{idx})$.

From plots in Figure 9, we can observe that the mean-point association strategy (Ours+SLC) leads to a more accurate localization of the landmarks with respect to the classic nearest-neighbor solution (NRF+NN+SLC). As discussed in Section 4.1.1, the mean-point association helps in preventing the landmarks to get attached to the closest point, which could not be the optimal choice especially when the difference between the template and the target is large. A qualitative example of this behavior is depicted in Figure 10: For large expressions or slight pose variations, the nearest-neighbor strategy cannot properly adapt to the global shape.

Consistently with other outcomes reported in the literature, the NICP solution provides competitive results on FRGCv2.0, but struggles when more complex expressions are considered as in Bosphorus or FaceWarehouse. The CPD



Fig. 11. Fitted shapes S (first, fourth columns) and the corresponding ground-truth faces (second, fifth columns). FRGCv2.0 (first row), Bosphorus (middle row) and FaceWarehouse (bottom row). The error heatmaps show the distribution of the per-vertex error.

algorithm, instead, performs badly in all the cases. The NICP and CPD are general solutions that can be applied to any 3D shape. In the case of human faces, having a statistical shape prior clearly helps in performing a meaningful fitting.

Finally, we compare our SLC solution against different methods for learning the 3DMM components. All the three approaches in conjunction with the mean-point association attain pretty accurate detections on all the datasets, with SLC performing best on FRGCv2.0 and FaceWarehouse, and DL on Bosphorus. Consistently with the analysis reported in [8], the DL better handles expressions with respect to PCA. The higher accuracy on Bosphorus can be ascribed to the similarity of the expressions contained in the latter and in the training scans (BU-3DFE). When dealing with different movements as those contained in FaceWarehouse, SLC-3DMM performs better, demonstrating the improved generalization capabilities to complex and new expressions. Some examples of fitting results are shown in Figure 11.

5.4.1 Comparison with state-of-the-art

In this section, we compare our approach with some state-of-the-art works for the detection of landmarks on the FRGCv2.0 and Bosphorus. Though our approach was not specifically tailored for landmark detection, we believe it is relevant to assess to what extent it is accurate in such task. Results for the compared approaches have been collected from the original papers.

TABLE 2

FRGCv2.0: Landmark localization error (mm). **Ex/En**-outer/inner eye corner, **N**-nose bridge, **Prn**-nose-tip, **Sn**-nasal base, **Ac**-nose corner, **Ch**-mouth corner, **Ls/Li**-upper/lower lip. Landmarks for Ex-En-Ch-Ac have been averaged. Best results in bold, second best in italic.

Method	Ex	En	N	Prn	Sn	Ac	Ch	Ls	Li	Avg
Creusot <i>et al.</i> [14]	5.9 ± 3.1	4.3 ± 2.2	4.2 ± 2.1	3.4 ± 2.0	3.7 ± 3.1	4.8 ± 3.6	5.6 ± 3.5	4.2 ± 3.2	5.5 ± 3.3	4.6 ± 2.9
BFM [61]	2.5 ± 2.2	2.7 ± 2.2	3.2 ± 2.2	2.3 ± 2.0	3.8 ± 3.6	8.3 ± 2.9	2.6 ± 2.9	2.6 ± 2.2	3.8 ± 3.7	3.5 ± 2.7
Sukno <i>et al.</i> [62]	4.7 ± 2.7	3.6 ± 1.7	2.5 ± 1.6	2.3 ± 1.7	2.7 ± 1.1	2.6 ± 1.4	3.9 ± 2.8	3.3 ± 1.8	4.6 ± 3.4	3.3 ± 2.0
K3DM _{BU} [33]	2.5 ± 2.2	2.4 ± 1.9	2.8 ± 1.8	2.6 ± 1.6	3.6 ± 1.9	6.1 ± 2.7	4.2 ± 3.1	2.9 ± 3.4	4.6 ± 2.9	3.5 ± 2.2
K3DM _{FR} [33]	2.5 ± 1.9	2.4 ± 1.2	2.5 ± 1.5	2.2 ± 1.8	3.4 ± 1.1	3.0 ± 2.4	2.5 ± 1.8	2.4 ± 3.1	3.5 ± 3.7	2.7 ± 2.0
Ours+PCA	4.0 ± 1.8	3.3 ± 1.4	2.1 ± 1.6	1.9 ± 1.0	1.4 ± 1.4	3.5 ± 1.2	4.5 ± 2.2	2.8 ± 1.4	3.6 ± 2.1	3.0 ± 1.6
Ours+DL [8]	3.9 ± 1.8	3.1 ± 1.3	2.1 ± 1.6	1.8 ± 1.0	1.4 ± 1.3	3.1 ± 1.1	4.1 ± 2.0	2.7 ± 1.4	3.5 ± 2.0	2.9 ± 1.6
Ours+SLC	3.8 ± 1.8	3.0 ± 1.3	1.8 ± 1.5	1.9 ± 1.0	1.5 ± 1.5	2.9 ± 1.2	4.2 ± 2.2	2.8 ± 1.5	3.6 ± 2.1	2.8 ± 2.1
Fan <i>et al.</i> [19]	2.1 ± 1.9	1.9 ± 1.0	2.4 ± 1.2	1.8 ± 1.2	1.8 ± 0.9	1.9 ± 0.9	2.8 ± 2.5	2.0 ± 2.2	4.3 ± 3.1	2.3 ± 1.5
Liu <i>et al.</i> [46]	1.9 ± 0.9	1.7 ± 0.9	2.7 ± 1.4	2.4 ± 1.4	-	-	2.6 ± 2.6	2.7 ± 2.7	4.0 ± 3.9	2.5 ± 1.9

Methods of [19], [46] use different settings, and so are not directly compared

TABLE 3

Bosphorus: Landmarks localization error (mm). **Ex/En**-outer/inner eye corner, **N**-nose bridge, **Prn**-nose-tip, **Sn**-nasal base, **Ac**-nose corner, **Ch**-mouth corner, **Ls/Li**-upper/lower lip. Landmarks for Ex-En-Ch-Ac have been averaged. Best results in bold, second best in italic.

Method	Ex	En	N	Prn	Sn	Ac	Ch	Ls	Li	Avg
Cruesot <i>et al.</i> [14]	$5.2 \pm \star$	$4.6 \pm \star$	$6.3 \pm \star$	$4.5 \pm \star$	$15.2 \pm \star$	$4.1 \pm \star$	$6.0 \pm \star$	$6.5 \pm \star$	$6.5 \pm \star$	$6.3 \pm \star$
BFM [61]	$3.6 \pm \star$	$2.7 \pm \star$	$2.2 \pm \star$	$2.9 \pm \star$	$3.6 \pm \star$	$4.0 \pm \star$	$5.9 \pm \star$	$4.0 \pm \star$	$6.5 \pm \star$	$3.9 \pm \star$
Sukno <i>et al.</i> [62]	$5.1 \pm \star$	$2.8 \pm \star$	$2.2 \pm \star$	$2.3 \pm \star$	$2.8 \pm \star$	$3.0 \pm \star$	$6.1 \pm \star$	$5.3 \pm \star$	$5.3 \pm \star$	$4.3 \pm \star$
K3DM _{BO} [33]	$3.6 \pm \star$	$2.5 \pm \star$	$2.3 \pm \star$	$2.8 \pm \star$	$2.3 \pm \star$	$2.7 \pm \star$	$4.9 \pm \star$	$3.3 \pm \star$	$5.0 \pm \star$	$3.3 \pm \star$
Ours+PCA	4.1 ± 2.2	3.0 ± 1.5	2.0 ± 1.2	2.1 ± 1.4	1.8 ± 1.9	3.8 ± 1.6	5.1 ± 2.8	3.3 ± 1.8	4.0 ± 3.0	3.2 ± 1.9
Ours+DL [8]	3.8 ± 2.0	2.7 ± 1.4	1.7 ± 1.1	2.1 ± 1.3	1.8 ± 1.7	3.4 ± 1.4	4.7 ± 2.6	2.9 ± 1.7	4.0 ± 3.1	3.0 ± 1.9
Ours+SLC	3.9 ± 2.2	2.9 ± 1.5	1.5 ± 1.0	2.2 ± 1.4	1.8 ± 1.7	3.0 ± 1.5	5.2 ± 3.2	3.2 ± 2.0	4.6 ± 3.9	3.1 ± 1.9
DLIN [32]	$3.0 \pm \star$	$2.7 \pm \star$	$2.6 \pm \star$	$2.2 \pm \star$	$2.5 \pm \star$	$2.7 \pm \star$	$2.8 \pm \star$	$3.5 \pm \star$	$3.5 \pm \star$	$2.9 \pm \star$

* Standard deviations are not reported separately for the “Expressions” subset of the dataset.

The method of [32] uses different settings, and so is not directly compared

TABLE 4

FaceWarehouse: Mean \pm Std of landmark localization error (mm). **Ex/En**-outer/inner eye corner, **Prn**-nose-tip, **Sn**-nasal base, **Ac**-nose corner, **Ch**-mouth corner, **Ls/Li**-upper/lower lip. Left and right landmarks for Ex-En-Ch-Ac have been averaged. Best results in bold

Method	Ex	En	Prn	Sn	Ac	Ch	Ls	Li	Avg
CPD [60]	6.8 ± 3.2	5.3 ± 2.7	3.4 ± 1.5	6.4 ± 4.1	8.8 ± 4.7	14.1 ± 5.4	6.6 ± 3.2	9.6 ± 3.8	7.6 ± 3.6
NICP [24]	5.4 ± 3.0	3.4 ± 2.1	3.0 ± 1.9	3.6 ± 2.8	5.1 ± 4.3	7.3 ± 3.9	4.3 ± 2.7	5.5 ± 3.4	4.7 ± 1.5
Ours+PCA	5.2 ± 2.9	3.5 ± 2.2	2.8 ± 1.6	3.6 ± 2.8	6.6 ± 4.5	6.3 ± 3.4	3.7 ± 2.4	5.3 ± 3.9	4.6 ± 3.1
Ours+DL	5.1 ± 2.8	3.0 ± 1.9	2.6 ± 1.6	3.5 ± 2.7	6.1 ± 4.5	5.8 ± 3.2	3.4 ± 2.4	5.0 ± 3.9	4.3 ± 2.9
Ours+SLC	4.0 ± 2.4	2.7 ± 1.7	2.8 ± 1.7	3.4 ± 2.6	5.5 ± 4.5	5.9 ± 3.5	3.5 ± 2.4	5.6 ± 4.6	4.1 ± 2.8

Table 2 reports results on the FRGCv2.0. Overall, the accuracy obtained using our approach attains comparable performance with respect to that reported by recent model-based approaches. We also included the results obtained by Liu *et al.* [46] and Fan *et al.* [19]. It is relevant here to comment about some significant differences between these methods and our approach. Liu *et al.* [46] employed a deep encoder-decoder network, which is trained on a massive amount of both fully registered synthetic scans and real scans. In particular, the FRGCv2.0 scans were included in their training data, which likely represents a bias in their experiments. Fan *et al.* [19], instead, employed a local-to-global registration strategy using a face template as starting point. They annotated a set of landmarks in the template and transferred the annotations to the target after template deformation, as we do. However, they used two different templates, one for neutral and another for expressive scans, while we have a unique, neutral average model. Moreover, they explicitly stated that due to inaccurate manual labeling on the template, the algorithm was applied to the neighboring points around a specified landmark. Eventually, the detected landmark was replaced by the neighboring

point with the minimum error. We still decided to include such methods in order to provide a complete overview of the most recent results in the field as reported in the literature. Table 2 shows that our approach can localize landmarks with sufficient precision, performing better than other model-based approaches. Further, note that this represents a challenging cross-dataset scenario as our SLC-3DMM is built from the registered scans of the BU-3DFE dataset obtained from [8]. In this regard, Gilani *et al.* [33] built their K3DM from different datasets. We report here the results of their K3DM built either from the BU-3DFE (K3DM_{BU}) or the FRGCv2.0 (K3DM_{FR}). Our approach outperforms the cross-database K3DM_{BU} model, while it performs comparably to K3DM_{FR}. The rather large accuracy difference between K3DM_{BU} and K3DM_{FR} suggests that a diversity between scans of different datasets actually exist, and can compromise the results of a template fitting algorithm to some extent. Our strategy allows to attenuate this problem, obtaining the same accuracy of the K3DM_{FR}.

Table 3 shows landmark detection results on the Bosphorus database. For the compared approaches, we reported the results obtained for the “Expression” subset, consisting

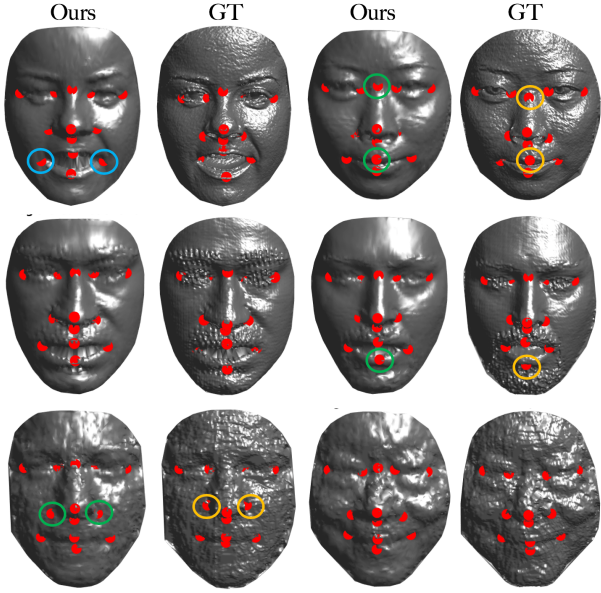


Fig. 12. Qualitative examples of landmark detection results on FRGCv2.0 (top row), Bosphorus (middle row), and FaceWarehouse (bottom row). Possible inaccurate manual labeling on the ground truth (yellow circles) are corrected by our semantic transfer (green circles). An example of inaccurate detection is also shown (blue circles). Note how the high-frequency surface details and noise are attenuated in our registered scans \hat{t}' , making them consistent across the datasets.

of 2,920 scans. Again, we report the outcome of the DLIN method [32] separately as it used a deep, fully convolutional network to detect the location of landmarks. With respect to the other approaches, our method performs better, demonstrating the good level of precision of the dense registration. It is also worth noting the results for K3DM_{BO} [33] are obtained using a model built on the same dataset, whereas we perform a cross-database evaluation.

We also report results on FaceWarehouse in Table 4. We cannot compare with other methods as, to the best of our knowledge, we are the first to perform 3D landmark detection on this dataset. Results are reported with respect to the landmark annotations provided therein. The annotations have been obtained by manually refining the detections of the Active Shape Model (ASM) detector [63]. Similar to the results reported in Figure 9, all the three methods perform competitively. In this dataset the point clouds are characterized by a high degree of noise and they also show particularly complex expressions. In such scenario, the advantage of using a sparse and localized solution turns out in a more evident way.

Some qualitative examples can be appreciated in Figure 12. From the examples, two major traits come up: First, the local consistency of motion and the good fitting accuracy allow refining possible inaccuracies in the manual labeling, which makes the annotation consistent across the scans; Second, we note dataset-specific surface details and noise are attenuated to a large extent in the re-indexed models \hat{t}' . More examples can be found in the supplemental material. Many of the compared works [19], [33], [62] correctly pointed out the importance of maintaining the mesh structure accurate and consistent across scans. However, this limits the opportunity to mix together scans with diverse

structures as could result from different capturing devices. Our solution allows overcoming this issue by transferring the structure of the fitted template. Finally, we wish to remark that all the reported detection results are obtained while also performing the dense registration; the two tasks are instead addressed separately in the compared works.

5.5 Heterogeneous Large-scale Morphable Model

One of the key aspects characterizing a 3DMM is that the more variability is contained in the training data, the more powerful and descriptive the model. However, collecting a large and sufficiently variegated set of densely registered scans is a very challenging task. Solutions in the literature commonly put a huge effort in collecting the data manually [25]. However, this solution has clear limitations. The data collection is a heavily cumbersome procedure not always possible that can take a very large amount of time and human effort. Still, putting the scans in dense correspondence heavily depends on the accuracy of the registration algorithm. Our proposed solution aims at overcoming these limitations and allows using a unique model to put in dense correspondence scans from, potentially, any dataset already collected, regardless of the specific characteristics of the capturing device, resolution, presence of unseen expressions or identities. Moreover, it effectively allows putting in dense correspondence scans with complex, non-standard expressions, which further enhances the representation power of the morphable model that is built from them. The only previous work that shows this capability is the method proposed by Liu *et al.* [46], who employed a deep learning framework, showing remarkable and promising results. However, if the target scans are not included in their training set, hence resembling a cross-dataset scenario, the performance degrades. Differently, we experimented our solutions exclusively in cross-dataset scenarios. Finally, we argue that the possibility of handling low-resolution scans as provided by consumer-like scanners such as Kinect is a valuable possibility, not only limited to the purpose of building a large set of fully registered models. The capability of accurately transferring the semantic annotation of a 3DMM to Kinect scans, as those of FaceWarehouse, allows further manipulations such as animation or expressions transfer.

Using the proposed dense registration algorithm, we put in dense correspondence scans of FRGCv2.0, Bosphorus and FaceWarehouse, and build our *Heterogeneous Large Scale Morphable Model* (HLS-3DMM). We considered all the available scans, for a total of 9,927 training samples, that comprise 721 individuals, with posed and spontaneous facial expressions, and a large variability in terms of age and ethnicity. Furthermore, since the scans are densely registered by transferring the semantic annotation provided by the SLC-3DMM, the registered scans of the BU-3DFE as provided in [8] could also be included in the training set of the HLS-3DMM, finally resulting in 11,570 fully registered samples. In the following evaluation, we will not consider this latter case in order not to bias the results. To evaluate the intrinsic characteristics of HLS-3DMM and jointly assess the accuracy of the dense registration, we follow a common practice in the literature of statistical shape models and use *compactness*, *generalization* and *specificity* measures [64]. In

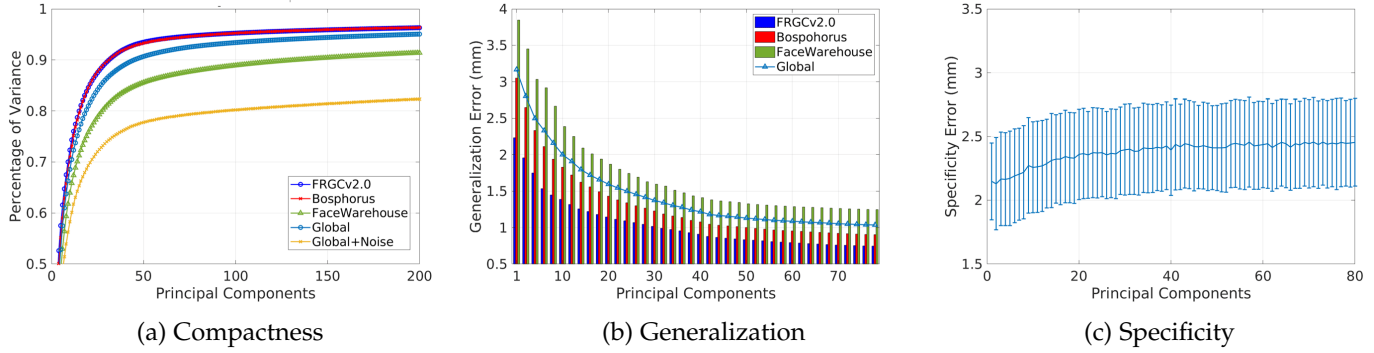


Fig. 13. Compactness, generalization and specificity measures for the HLS-3DMM constructed from 9,927 registered scans.

order to discuss the outcomes fairly with respect to other models reported in the literature, we followed the standard practice and built the HLS-3DMM by applying PCA to the registered scans. Note that, because of the possibly significant differences among the employed data, a direct comparison with other works is not possible; for the sake of completeness, we will still comment and discuss the outcomes with respect to other previous works.

5.5.1 Compactness

Compactness measures the percentage of variance of the training data that is explained by a model when a certain number of principal components are retained. For a morphable face model, this clearly depends on two factors: (*i*) how faithfully and precisely the dense registration algorithm captured the real data distribution; (*ii*) the variance contained in the training data, *i.e.*, number of identities, presence of expressions, ethnicity, age, etc. In Figure 13 (a), we report the plots of the HLS-3DMM, comparing the model constructed from all the available registered scans, and three sub-models built from FRGCv2.0, Bosphorus and FaceWarehouse separately. The global model can be considered sufficiently compact; It can explain more than 90% of the variance with as few as 50 principal components. This result is consistent with other large scale models reported in the literature. For example, in [65], the same variance is retained with approximately 40 components. Being the number of training samples similar ($\approx 10,000$), their data contain around 9,000 identities collected from the same device, but no expressions. Our training set has 471 identities but contains much more variabilities in terms of posed and natural facial expressions, asymmetric action units and different capturing devices.

When comparing the sub-models, we can see that those learned on FRGCv2.0 and Bosphorus have almost overlapping compactness curves, retaining the 90% of the variance with the first 30 principal components. This makes sense, also with respect to [65], in as much as the former includes 466 identities but few expressions, while the latter consists of only 105 subjects, each one with a large number of different expressions. The FaceWarehouse model, instead, demonstrates less compact. This can be ascribed to the very spontaneous nature of the expressions, but mostly to the prominent noise. However, if we corrupt the training data with noise drawn from the standard normal distribution

$\mathcal{N}(0, 1)$ and re-compute the compactness, it results significantly lower, demonstrating that the dense registration was performed fairly accurately.

Finally, we point out that including such noisy scans in the training set of a morphable model is not the best choice. However, many solutions exist to reduce the noise of a low-cost scanner if multiple frames are available, *e.g.*, using Kinect Fusion as in [37], or the method of Bondi *et al.* [66]. Unfortunately, the publicly available data of FaceWarehouse included only the first frame. Nonetheless, this served us to showcase the capability of our algorithm to work accurately also in very critical conditions, making it suitable as a general purpose method for detecting landmarks.

5.5.2 Generalization

Generalization measures the ability of the model to represent novel instances of face shapes that are unseen during training. To this aim, following the standard practice, we split the registered scans into a train and a test set. The test set is composed of 300 scans, chosen randomly and in equal proportion from the three datasets, *i.e.*, 100 from FRGCv2.0, 100 from Bosphorus and 100 from FaceWarehouse, to guarantee sufficient diversity. We further ensured identities between train and test do not overlap. The HLS-3DMM is built applying PCA to the reduced training set. To compute the generalization error, for each shape in the test set, we estimate the deformation coefficients α using (9), and deform the average model using (1). The error is computed as the mean per-vertex Euclidean distance. In Figure 13 (b), the average generalization error over all the test set is reported as well as the error obtained on the three subsets separately. We observe the capability of HLS-3DMM to generalize well to unseen samples, also considering other results reported in the recent literature [9], [48], [67]. Other than the global average, we report results separately for each dataset to assess the different behavior. The FRGCv2.0 samples obtain the lowest error, likely because of the limited number of samples showing strong expressions. An interesting trend that can be observed is the gap between FRGC and the expressive scans of Bosphorus reducing as the number of components grows, indicating the model capability of capturing and reproducing facial expressions. The larger error on FaceWarehouse, instead, indicates that the model is, desirably, not reproducing high-frequency noise patterns.

5.5.3 Specificity

Specificity evaluates the validity of synthetic faces generated by the model. We randomly generated 1,000 synthetic faces for a fixed number of principal components and measured how close they are from the samples in the test set. For each synthetic face, we found the sample in the test set with minimum error in terms of (average) per-vertex Euclidean distance. The curve in Figure 13 (c) reports the average of this error across all the synthetic faces, along with the standard deviation. In comparison with other works, we attain good specificity error. For example, Booth *et al.* [9] reported a specificity error varying from 1 to 1.8mm on a test set of neutral models only; Dai *et al.* [67], instead, reported errors varying from 2.6 to 3.5mm for their cranio-facial model. Our model is capable of generating realistic faces, which also include facial expressions. As a desirable behavior achieved by our model, we observe the error remains stable even for a larger number of principal components.

5.5.4 Manipulating Registered Faces

Another common way to qualitatively assess the fidelity of a dense registration algorithm consists in manipulating the registered 3D faces. We show our sparse SLC components can be exploited to apply localized facial deformations to arbitrary registered scans. To this aim, we learn the SLC components as described in Section 3 from the newly registered 9,927 scans. Then, we take some sample registered scans and deform them by applying randomly chosen SLC components (each deformation is obtained using a single component). In Figure 14 some examples are shown. We can observe local areas are smoothly deformed with realistic and natural facial movements. Thanks to the new and complex expressions included in the training scans, we are also capable of reproducing asymmetric as well as natural and realistic facial movements. Further, the scans could also be manipulated by arbitrarily selecting one or more control points as described in Section 5.2.2. An additional qualitative analysis of both SLC and PCA latent spaces can be found in the supplemental material.

6 CONCLUSIONS

In this paper, we proposed a dense 3D face correspondence approach, which leverages a 3DMM to transfer a point-to-point semantic annotation across raw 3D faces. We proposed a novel Sparse Vertex Dictionary Learning formulation to learn sparse and locally coherent deformation components that are used to accurately fit the 3DMM also to new and unseen facial deformations. The fitting is guided by the proposed Non Rigid Fitting algorithm, specifically tailored for adapting to heterogeneous scans and large shape differences. The approach demonstrated to be accurate even in presence of strong facial expressions, and for very different types of 3D faces from multiple databases. We then densely registered together scans coming from three face databases, and built a large-scale, heterogeneous 3DMM from them, which exhibits remarkable modeling capabilities in terms of natural and complex facial movements. The very different and complementary characteristics of the considered databases suggest the approach can be used to further enlarge the set of registered scans to, potentially, any database



Fig. 14. Qualitative examples of local deformations applied to registered scans (middle column) by means of our SLC components.

already collected, which represents a valuable contribution that every 3DMM learning framework would benefit from.

However, the proposed SLC and NRF approaches are not exempt from limitations. For example, the need for a set of pre-registered scans to train the SLC-3DMM still represents the main constraint. Despite showing the SLC-3DMM can generalize better than other 3DMM learning techniques to complex and unseen deformations, a solution to further enhance this behavior would be beneficial. In this regard, future experimentations will involve learning the SLC-3DMM from synthetically generated scans only, ultimately making it a fully independent model. This would also allow increasing the resolution of the template. Generally, learning a 3DMM from synthetic scans is not desirable, as the face variability carried by the scans would be inherently limited by the specific generator. However, our SLC components demonstrated effective in expanding the modeling capabilities beyond those contained in the data by de-correlating facial movements. On the other hand, the NRF procedure showed some weaknesses, mostly in case of occlusions. Whereas we specifically did not address this issue in the light of our goal, we aim at improving the procedure to account for that.

REFERENCES

- [1] V. Blanz and T. Vetter, "A morphable model for the synthesis of 3D faces," in *ACM Conf. on Computer Graphics and Interactive Techniques*, 1999, pp. 187-194.
- [2] B. Amberg, R. Knothe, and T. Vetter, "Expression invariant 3D face recognition with a morphable model," in *IEEE Int. Conf. on Automatic Face and Gesture Recognition*, 2008.
- [3] V. Blanz and T. Vetter, "Face recognition based on fitting a 3D morphable model," *IEEE Trans. on Pattern Analysis and Machine Intelligence*, vol. 25, no. 9, pp. 1063-1074, 2003.

[4] S. Ramanathan, A. Kassim, Y. V. Venkatesh, and W. S. Wah, "Human facial expression recognition using a 3D morphable model," in *Int. Conf. on Image Processing*, 2006.

[5] X. Cao, Z. Chen, A. Chen, X. Chen, S. Li, and J. Yu, "Sparse photometric 3d face reconstruction guided by morphable models," in *IEEE/CVF Conf. on Computer Vision and Pattern Recognition (CVPR)*, 2018, pp. 4635–4644.

[6] T. Neumann, K. Varanasi, S. Wenger, M. Wacker, M. Magnor, and C. Theobalt, "Sparse localized deformation components," *ACM Trans. Graphics*, vol. 32, no. 6, pp. 179:1–179:10, 2013.

[7] F. C. Staal, A. J. Ponniah, F. Angullia, C. Ruff, M. J. Koudstaal, and D. Dunaway, "Describing crouzon and pfeiffer syndrome based on principal component analysis," *Journal of Cranio-Maxillofacial Surgery*, vol. 43, no. 4, pp. 528–536, 2015.

[8] C. Ferrari, G. Lisanti, S. Berretti, and A. Del Bimbo, "A dictionary learning-based 3D morphable shape model," *IEEE Trans. on Multimedia*, vol. 19, no. 12, pp. 2666–2679, 2017.

[9] J. Booth, A. Roussos, A. Ponniah, D. Dunaway, and S. Zafeiriou, "Large scale 3D morphable models," *Int. Journal of Computer Vision*, vol. 126, no. 2, pp. 233–254, 2017.

[10] M. Lathi, T. Gerig, C. Jud, and T. Vetter, "Gaussian process morphable models," *IEEE Trans. on Pattern Analysis and Machine Intelligence*, vol. 40, no. 8, pp. 1860–1873, 2018.

[11] C. Ferrari, S. Berretti, P. Pala, and A. Del Bimbo, "3DMM for accurate reconstruction of depth data," in *Int. Conf. on Image Analysis and Processing (ICIAP)*, 2019, pp. 532–543.

[12] —, "3D face reconstruction from RGB-D data by morphable model to point cloud dense fitting," in *Int. Conf. on Pattern Recognition Applications and Methods (ICPRAM)*, 2019, pp. 728–735.

[13] —, "Rendering realistic subject-dependent expression images by learning 3dmm deformation coefficients," in *European Conf. on Computer Vision Workshop (ECCVW)*, vol. 11130, 2019, pp. 441–455.

[14] C. Creusot, N. Pears, and J. Austin, "A machine-learning approach to keypoint detection and landmarking on 3D meshes," *Int. Journal of Computer Vision*, vol. 102, no. 1-3, pp. 146–179, 2013.

[15] X. Lu and A. K. Jain, "Automatic feature extraction for multiview 3D face recognition," in *IEEE Int. Conf. on Automatic Face and Gesture Recognition (FGR)*, 2006, pp. 585–590.

[16] M. Pamplona Segundo, L. Silva, O. R. P. Bellon, and C. C. Queirolo, "Automatic face segmentation and facial landmark detection in range images," *IEEE Trans. on Systems, Man, and Cybernetics, Part B (Cybernetics)*, vol. 40, no. 5, pp. 1319–1330, 2010.

[17] P. Perakis, G. Passalis, T. Theoharis, and I. A. Kakadiaris, "3D facial landmark detection under large yaw and expression variations," *IEEE Trans. on Pattern Analysis and Machine Intelligence*, vol. 35, no. 7, pp. 1552–1564, 2013.

[18] P. Perakis, T. Theoharis, and I. A. Kakadiaris, "Feature fusion for facial landmark detection," *Pattern Recognition*, vol. 47, no. 9, pp. 2783–2793, 2014.

[19] Z. Fan, X. Hu, C. Chen, and S. Peng, "Boosting local shape matching for dense 3D face correspondence," in *IEEE/CVF Conf. on Computer Vision and Pattern Recognition (CVPR)*, 2019, pp. 10936–10946.

[20] A. Salazar, S. Wuhrer, C. Shu, and F. Prieto, "Fully automatic expression-invariant face correspondence," *Machine Vision and Applications*, vol. 25, pp. 859–879, 2014.

[21] Y. Sun and M. A. Abidi, "Surface matching by 3d point's fingerprint," in *IEEE Int. Conf. on Computer Vision (ICCV)*, vol. 2, 2001, pp. 263–269.

[22] Y. Zeng, C. Wang, X. Gu, D. Samaras, and N. Paragios, "Higher-order graph principles towards non-rigid surface registration," *IEEE Trans. on Pattern Analysis and Machine Intelligence*, vol. 38, no. 12, pp. 2416–2429, 2016.

[23] Y. Zeng, C. Wang, Y. Wang, X. Gu, D. Samaras, and N. Paragios, "Dense non-rigid surface registration using high-order graph matching," in *IEEE Conf. on Computer Vision and Pattern Recognition (CVPR)*, 2010, pp. 382–389.

[24] B. Amberg, S. Romdhani, and T. Vetter, "Optimal step nonrigid ICP algorithms for surface registration," in *IEEE Conf. on Computer Vision and Pattern Recognition (CVPR)*, 2007, pp. 1–8.

[25] J. Booth, A. Roussos, S. Zafeiriou, A. Ponniah, and D. Dunaway, "A 3D morphable model learnt from 10,000 faces," in *IEEE Conf. on Computer Vision and Pattern Recognition*, 2016, pp. 5543–5552.

[26] H. Li, R. W. Sumner, and M. Pauly, "Global correspondence optimization for non-rigid registration of depth scans," *Computer Graphics Forum*, vol. 27, no. 5, pp. 1421–1430, 2008.

[27] B. Maiseli, Y. Gu, and H. Gao, "Recent developments and trends in point set registration methods," *Journal of Visual Communication and Image Representation*, vol. 46, pp. 95 – 106, 2017.

[28] G. K. L. Tam, Z. Cheng, Y. Lai, F. C. Langbein, Y. Liu, D. Marshall, R. R. Martin, X. Sun, and P. L. Rosin, "Registration of 3D point clouds and meshes: A survey from rigid to nonrigid," *IEEE Trans. on Visualization and Computer Graphics*, vol. 19, no. 7, pp. 1199–1217, 2013.

[29] O. van Kaick, H. Zhang, G. Hamarneh, and D. Cohen-Or, "A survey on shape correspondence," *Computer Graphics Forum*, vol. 30, no. 6, pp. 1681–1707, 2011.

[30] P. Paysan, R. Knothe, B. Amberg, S. Romdhani, and T. Vetter, "A 3D face model for pose and illumination invariant face recognition," in *IEEE Int. Conf. on Advanced Video and Signal Based Surveillance (AVSS)*, 2009, pp. 296–301.

[31] S. Z. Gilani, F. Shafait, and A. Mian, "Shape-based automatic detection of a large number of 3d facial landmarks," in *IEEE Conf. on Computer Vision and Pattern Recognition (CVPR)*, 2015, pp. 4639–4648.

[32] S. Z. Gilani, A. Mian, and P. Eastwood, "Deep, dense and accurate 3d face correspondence for generating population specific deformable models," *Pattern Recognition*, vol. 69, pp. 238–250, 2017.

[33] S. Z. Gilani, A. Mian, F. Shafait, and I. Reid, "Dense 3D face correspondence," *IEEE Trans. on Pattern Analysis and Machine Intelligence*, vol. 40, no. 7, pp. 1584–1598, 2018.

[34] Z. Fan, X. Hu, C. Chen, and S. Peng, "Dense semantic and topological correspondence of 3D faces without landmarks," in *European Conf. on Computer Vision (ECCV)*, vol. 11220, 2018, pp. 541–558.

[35] J. Yang, H. Li, D. Campbell, and Y. Jia, "Go-icp: A globally optimal solution to 3D ICP point-set registration," *IEEE Trans. on Pattern Analysis and Machine Intelligence*, vol. 38, no. 11, pp. 2241–2254, 2016.

[36] J. Yang, H. Li, and Y. Jia, "Go-icp: Solving 3D registration efficiently and globally optimally," in *IEEE Int. Conf. on Computer Vision*, 2013, pp. 1457–1464.

[37] C. Cao, Y. Weng, S. Zhou, Y. Tong, and K. Zhou, "Facewarehouse: A 3D facial expression database for visual computing," *IEEE Trans. on Visualization and Computer Graphics*, vol. 20, no. 3, pp. 413–425, 2014.

[38] A. Patel and W. A. P. Smith, "3D morphable face models revisited," in *IEEE Conf. on Computer Vision and Pattern Recognition (CVPR)*, 2009, pp. 1327–1334.

[39] A. Brunton, T. Bolkart, and S. Wuhrer, "Multilinear wavelets: A statistical shape space for human faces," in *European Conf. on Computer Vision*, 2014, pp. 297–312.

[40] C. Chen, L. B. Hensel, Y. Duan, R. A. Ince, O. G. Garrod, J. Beskow, R. E. Jack, and P. G. Schyns, "Equipping social robots with culturally-sensitive facial expressions of emotion using data-driven methods," in *IEEE Int. Conf. on Automatic Face & Gesture Recognition (FG)*, 2019, pp. 1–8.

[41] S. Sengupta, A. Kanazawa, C. D. Castillo, and D. W. Jacobs, "Sfsnet: Learning shape, reflectance and illuminance of faces in the wild," in *IEEE Conf. on Computer Vision and Pattern Recognition (CVPR)*, 2018, pp. 6296–6305.

[42] T. Bagautdinov, C. Wu, J. Saragih, P. Fua, and Y. Sheikh, "Modeling facial geometry using compositional vaes," in *IEEE Conf. on Computer Vision and Pattern Recognition (CVPR)*, 2018, pp. 3877–3886.

[43] A. Ranjan, T. Bolkart, S. Sanyal, and M. Black, "Generating 3D faces using convolutional mesh autoencoders," in *European Conf. on Computer Vision (ECCV)*, vol. 11207, 2018, pp. 725–741.

[44] Z.-H. Jiang, Q. Wu, K. Chen, and J. Zhang, "Disentangled representation learning for 3D face shape," in *IEEE Conf. on Computer Vision and Pattern Recognition (CVPR)*, June 2019, pp. 11 957–11 966.

[45] T. Li, T. Bolkart, M. J. Black, H. Li, and J. Romero, "Learning a model of facial shape and expression from 4D scans," *ACM Trans. on Graphics*, vol. 36, no. 6, pp. 194:1–194:17, 2017.

[46] F. Liu, L. Tran, and X. Liu, "3d face modeling from diverse raw scan data," in *IEEE/CVF Int. Conf. on Computer Vision (ICCV)*, 2019, pp. 9407–9417.

[47] R. Q. Charles, H. Su, M. Kaichun, and L. J. Guibas, "Pointnet: Deep learning on point sets for 3D classification and segmentation," in *IEEE Conf. on Computer Vision and Pattern Recognition (CVPR)*, 2017, pp. 77–85.

[48] S. Ploumpis, H. Wang, N. Pears, W. A. Smith, and S. Zafeiriou, "Combining 3D morphable models: A large scale face-and-head

model," in *IEEE Conf. on Computer Vision and Pattern Recognition (CVPR)*, 2019, pp. 10934–10943.

[49] H. Dai, N. Pears, W. Smith, and C. Duncan, "A 3d morphable model of craniofacial shape and texture variation," in *IEEE Int. Conf. on Computer Vision (ICCV)*, 2017, pp. 3104–3112.

[50] J. Mairal, F. Bach, J. Ponce, and G. Sapiro, "Online learning for matrix factorization and sparse coding," *Journal of Machine Learning Research*, vol. 11, pp. 19–60, 2010.

[51] ———, "Online dictionary learning for sparse coding," in *Int. Conf. on Machine Learning*, 2009, pp. 689–696.

[52] G. Pan, X. Zhang, Y. Wang, Z. Hu, X. Zheng, and Z. Wu, "Establishing point correspondence of 3D faces via sparse facial deformable model," *IEEE Trans. on Image Processing*, vol. 22, no. 11, pp. 4170–4181, 2013.

[53] P. J. Phillips, P. J. Flynn, T. Scruggs, K. W. Bowyer, J. Chang, K. Hoffman, J. Marques, J. Min, and W. Worek, "Overview of the face recognition grand challenge," in *IEEE Work. on Face Recognition Grand Challenge Experiments*, Jun. 2005, pp. 947–954.

[54] A. Savran, N. Alyüz, H. Dibeklioğlu, O. Çeliktutan, B. Gökberk, B. Sankur, and L. Akarun, "Bosphorus database for 3D face analysis," in *Proc. First COST 2101 Work. on Biometrics and Identity Management*, May 2008.

[55] C. Cao, Y. Weng, S. Zhou, Y. Tong, and K. Zhou, "Facewarehouse: A 3D facial expression database for visual computing," *IEEE Transactions on Visualization and Computer Graphics*, vol. 20, no. 3, pp. 413–425, 2013.

[56] L. Yin, X. Wei, Y. Sun, J. Wang, and M. J. Rosato, "A 3D facial expression database for facial behavior research," in *IEEE Int. Conf. on Automatic Face and Gesture Recognition (FG)*, 2006, pp. 211–216.

[57] A. Bulat and G. Tzimiropoulos, "How far are we from solving the 2d & 3d face alignment problem? (and a dataset of 230,000 3d facial landmarks)," in *Int. Conf. on Computer Vision (ICCV)*, 2017.

[58] D. Kim, M. Hernandez, J. Choi, and G. Medioni, "Deep 3d face identification," in *IEEE Int. Joint Conf. on Biometrics (IJCB)*, 2017, pp. 133–142.

[59] O. M. Parkhi, A. Vedaldi, and A. Zisserman, "Deep face recognition," in *British Machine Vision Conf. (BMVC)*, 2015.

[60] A. Myronenko and X. Song, "Point set registration: Coherent point drift," *IEEE Trans. on Pattern Analysis and Machine Intelligence*, vol. 32, no. 12, pp. 2262–2275, 2010.

[61] P. Paysan, R. Knothe, B. Amberg, S. Romdhani, and T. Vetter, "A 3d face model for pose and illumination invariant face recognition," in *IEEE Int. Conf. on Advanced Video and Signal Based Surveillance (AVSS)*, 2009, pp. 296–301.

[62] F. M. Sukno, J. L. Waddington, and P. F. Whelan, "3-d facial landmark localization with asymmetry patterns and shape regression from incomplete local features," *IEEE Trans. on Cybernetics*, vol. 45, no. 9, pp. 1717–1730, 2014.

[63] T. F. Cootes, C. J. Taylor, D. H. Cooper, and J. Graham, "Active shape models-their training and application," *Computer Vision and Image Understanding*, vol. 61, no. 1, pp. 38–59, 1995.

[64] R. Davies, C. Twining, and C. Taylor, *Statistical models of shape: Optimisation and evaluation*. Springer Science & Business Media, 2008.

[65] J. Booth, E. Antonakos, S. Ploumpis, G. Trigeorgis, Y. Panagakis, and S. Zafeiriou, "3D face morphable models "in-the-wild"," in *IEEE Conf. on Computer Vision and Pattern Recognition (CVPR)*, 2017, pp. 5464–5473.

[66] E. Bondi, P. Pala, S. Berretti, and A. Del Bimbo, "Reconstructing high-resolution face models from kinect depth sequences," *IEEE Trans. on Information Forensics and Security*, vol. 11, no. 12, pp. 2843–2853, 2016.

[67] H. Dai, N. Pears, W. A. Smith, and C. Duncan, "A 3d morphable model of craniofacial shape and texture variation," in *IEEE Int. Conf. on Computer Vision (ICCV)*, 2017, pp. 3085–3093.



Claudio Ferrari received the Ph.D. in Information Engineering from the University of Florence in 2018. Currently, he is a postdoctoral researcher at the Media Integration and Communication Center (MICC) of the University of Florence. He has been a visiting research scholar at the University of Southern California (USC) in 2014. His research interests focus on computer vision and machine learning for biometrics and 2D/3D face analysis.



Stefano Berretti received the Ph.D. in Computer Engineering in 2001. Currently, he is an Associate Professor at University of Florence, Italy. He has been Visiting Professor at University of Lille and University of Alberta. His research interests focus on computer vision for face biometrics, human emotion and behavior understanding, computer graphics and multimedia. He is the Information Director and an Associate Editor of the ACM Transactions on Multimedia Computing, Communications, and Applications, and Associate Editor of the IET Computer Vision journal.



Pietro Pala received the Ph.D. in Information and Telecommunications Engineering in 1997 at the University of Florence. Currently, he is Full Professor of Informatics Engineering at the School of Engineering of the University of Florence. His research activity focus on the use of pattern recognition models for multimedia information retrieval and biometrics, and on the study of 3D data for person and action recognition. He serves as editor for Multimedia Systems and ACM Transactions on Multimedia Computing, Communications, and Applications (TOMM).



Alberto Del Bimbo is Full Professor of Computer Engineering at the University of Florence, Italy. His scientific interests include multimedia information retrieval, pattern recognition, image and video analysis and natural humancomputer interaction. Prof. Del Bimbo is IAPR Fellow, Associate Editor of several leading journal in the area of pattern recognition and multimedia, and the Editor-in-Chief of the ACM Transactions on Multimedia Computing, Communications, and Applications. He was also the recipient of the prestigious SIGMM 2016 Award for Outstanding Technical Contributions to Multimedia Computing, Communications and Applications.